Journal Pre-proofs

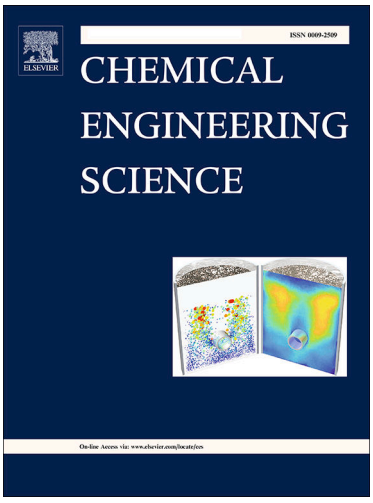

Modelling excited species and their role on kinetic pathways in the non-oxidative coupling of methane by dielectric barrier discharge

P.-A. Maitre, M.S. Bieniek, P.N. Kechagiopoulos

PII: S0009-2509(20)30931-3
DOI: https://doi.org/10.1016/j.ces.2020.116399
Reference: CES 116399

To appear in: *Chemical Engineering Science*

Received Date: 22 August 2020
Revised Date: 7 December 2020
Accepted Date: 19 December 2020

Please cite this article as: P.-A. Maitre, M.S. Bieniek, P.N. Kechagiopoulos, Modelling excited species and their role on kinetic pathways in the non-oxidative coupling of methane by dielectric barrier discharge, *Chemical Engineering Science* (2020), doi: https://doi.org/10.1016/j.ces.2020.116399

Modelling excited species and their role on kinetic pathways in the non-oxidative coupling of methane by dielectric barrier discharge

P.-A. Maitre, M. S. Bieniek, P. N. Kechagiopoulos*
Chemical and Materials Engineering Group, School of Engineering,
University of Aberdeen, Aberdeen, UK
* email: *p.kechagiopoulos@abdn.ac.uk*

Abstract

A detailed kinetic scheme for non-thermal methane plasma is developed that considers the reactivity and relaxation of electronically and vibrationally excited species. An atmospheric pressure dielectric barrier discharge reactor for methane non-oxidative coupling is modelled. Via 1D fluid modelling short periods of time are investigated, while for longer periods of time, on the order of the reactor residence time, a combined 1D-0D approach is followed. Modelling results are in good qualitative agreement with literature experiments. Around 86% of the energy input is found to channel into the creation of excited species. The vibrationally excited states of methane exhibit very transient responses due to their rapid formation during electron streamers and fast quenching by VV and VT processes. The, higher energy, electronically excited states are rapidly converted, many of which essentially instantly dissociate. Over 70% of methane's conversion proceeds via electronical excitation, while the contribution of vibrationally excited states is limited.

Keywords: non-thermal plasma; dielectric barrier discharge; non-oxidative methane coupling; excited states; kinetic modelling; energy channelling

1 Introduction

Large quantities of valuable chemicals, such as ethylene, are currently being produced by the non renewable and energy demanding cracking of crude oil fractions (Gilbert et al., 2013). A promising, and potentially more environmentally friendly, alternative route to these chemicals is via the upgrading of methane into higher hydrocarbons. Methane is widely available in natural gas, shale gas, and also increasingly obtainable from renewable bio-gas and landfill-gas. Direct conversion of methane into higher hydrocarbons can currently be achieved by oxidative coupling of methane (OCM) over a catalyst at high temperatures (Kechagiopoulos et al., 2014). The OCM process, however, generates carbon dioxide, requires high temperatures (800-1000 °C), and has relatively low C_2 yields (Lunsford, 2000). Non-direct routes, whereby methane is steam-reformed into syngas, and then, via the Fischer–Tropsch synthesis, converted into higher hydrocarbons are also available, but are energy-demanding, and tend to be expensive as they are complex, multi-step, processes (Wang et al., 2017).

Over the last two decades, plasma technologies, wherein methane gas is exposed to a, typically, electrically induced discharge, have been extensively studied as a way to activate methane in the absence of oxidants. The

electric field accelerates the naturally-present free electrons, which upon collision with methane molecules, form a variety of reactive species such as ions, excited states, and radicals. Subsequent coupling and chain propagation reactions within the plasma lead to the formation of C_2 and higher hydrocarbon species (Maitre et al., 2020, Scapinello et al., 2017). Plasma discharges can be operated under different conditions of temperature and pressure, at varying degree of deviation from thermal equilibrium. Some non-equilibrium plasmas, like gliding arcs, sparks, nanosecond pulsed discharges (Delikonstantis et al., 2020, Dors et al., 2014, Heijkers et al., 2020, Scapinello et al., 2019) or microwave discharges (Dors et al., 2014, Heijkers et al., 2020), operate at high gas temperature (>800K), while others, like corona (Yang, 2003a) or dielectric barrier discharges (DBD) (Nozaki and Okazaki, 2013, Saleem et al., 2019, Toth et al., 2018, Wang et al., 2013, Xu and Tu, 2013), operate at much lower gas temperature (generally below 500K).

In the presence of a catalyst, the plasma species can further be selectively converted towards higher hydrocarbons at higher yields than when the plasma is used alone, as described in detail in e.g. published reviews (Maitre et al., 2020, Nozaki and Okazaki, 2013, Puliyalil et al., 2018, Scapinello et al., 2017). This process confers significant benefits and is highly environmentally and economically relevant as it provides the potential to upgrade methane at low temperatures, using renewable electricity, in absence of oxygen containing by-products. The biggest challenge in plasma-catalysis systems affecting their further development is that the interactions between the two phases are numerous, and not well understood. Among many, the catalyst can be responsible for local field enhancement and micro-discharge formation in pores, while the plasma can increase the adsorption probability of species, as demonstrated in molecular beam (Juurlink et al., 2009), kinetic (Sheng et al., 2020) and modelling (Engelmann et al., 2020) studies, potentially lower the activation barrier of surface processes, and modify the catalyst surface area and functionality (Neyts, 2016, Whitehead, 2016). To this end, modelling can provide useful insights, allowing to probe the contribution of the complex reaction and transport mechanisms in a manner not easily accessible via solely experimentation.

To date, there has been no self-consistent modelling of the entire process, of the evolution of the gas phase, the plasma phase, and the catalyst surface processes (Khoja et al., 2019a). De Bie et al. (2011) performed modelling of the conversion of pure atmospheric pressure methane by dielectric barrier discharge (DBD), without the presence of a catalyst. A detailed kinetic network was developed in that work which was used in one-dimensional simulations. The simulation results presented the main reaction products as dihydrogen and ethane, which was consistent with experiments (Liu et al., 1998). The simulations described in a comprehensive manner the ground state neutral gas chemistry, but omitted the reactivity of electronically and vibrationally excited species, as well as negative ions. Through step-wise and direct energy transfer processes, excited species can facilitate ionisation and dissociation of molecules (Fridman, 2008, Koelman et al., 2017, Kozák and Bogaerts, 2014, Snoeckx and Bogaerts, 2017, Snoeckx et al., 2013, Sun and Chen, 2019). Further, vibrational energy can effectively contribute to the overcoming of

activation barriers in endothermic chemical reactions (Rusanov et al., 1981). Thus, when the production of excited species is high, their role in the plasma reactivity may be significant.

The reactivity of the excited species has not been considered in the majority of previous modelling work on the upgrading of pure methane by dielectric barrier discharges (De Bie et al., 2011, Indarto et al., 2008, Khadir et al., 2017, Yang, 2003b). Of all published modelling studies on low temperature methane plasmas (Agiral et al., 2008, Bera et al., 1999, 2001, Bleecker et al., 2003, De Bie et al., 2011, Efremov et al., 2015, Fan et al., 1999, Ferrara et al., 2012, Gogolides et al., 1994, Herrebout et al., 2001, 2002, Indarto et al., 2008, Khadir et al., 2017, Kraus et al., 2002, Kudryashov et al., 2018, Liu et al., 1998, Luche et al., 2009, Masi et al., 1998, Naidis, 2007, 2018, Pintassilgo et al., 2007, Pourali and Foroutan, 2015, Qian et al., 2018, Snoeckx et al., 2013, Sun and Chen, 2019, Tachibana et al., 1984, Wang et al., 2018, Yang, 2003b, Yarin et al., 2006, Yoon et al., 2001), the reactivity of vibrationally excited states was accounted for by Sun and Chen (2019), who performed zero-dimensional modelling of methane upgrading via radio-frequency plasma. The results indicated that, indeed, a significant amount of vibrationally excited states is produced, with around 40% of the conversion of methane proceeding via vibrationally excited methane. More recently, Heijkers et al. (2020) used zero-dimensional models to study the reaction mechanism and energy efficiency of various plasma sources, during methane upgrading, accounting for the reactivity of vibrationally excited methane and hydrogen. The contribution of these states on the kinetic pathways was not specifically discussed, although it was commented that for all plasmas, including DBD, vibrational-translational non-equilibrium was negligible.

Despite the low energy efficiency of DBDs in comparison to spark and pulsed discharges (Maitre et al., 2020, Nozaki and Okazaki, 2013, Puliyalil et al., 2018, Scapinello et al., 2017), the low operating temperature and co-axial reactor configuration typically employed to generate this type of discharge make it particularly suited for kinetic and catalyst evaluation studies in packed beds, justifying its extensive use in recent plasma-catalysis experimental literature (Khoja et al., 2018, 2019a,b, Michielsen et al., 2019, Nozaki and Okazaki, 2013, Ray et al., 2019), facilitating as such model validation. In this paper a regular one-dimensional dielectric barrier discharge fluid model is used in combination with a zero-dimensional flow reactor model in order to simulate the methane upgrading process, without the presence of a catalyst. A detailed kinetic scheme of low temperature methane plasma is developed that includes processes involving electronically and vibrationally excited species, and negative ions. The modelling results are in good qualitative agreement with the experiments in the literature in terms of methane conversion and product selectivities. The results and analysis highlight the substantial and interesting role of both electronically and vibrationally excited species in the conversion process. The present model by considering explicitly the excited states in the plasma phase further enables the future development of plasma-catalytic microkinetic models accounting for the interactions of all plasma species with the catalyst surface, the validation of such models benefiting greatly from the wealth of plasma-catalysis experimental data already available in DBD reactors.

The outline of the paper is as follows. In Section 2, the kinetic scheme developed and used in this work is described. In Section 3 the numerical models are described. In Section 4 results from the modelling are presented

and discussed. Conclusions are drawn and directions of future work are discussed in Section 5.

2 The kinetic scheme

In developing the detailed kinetic scheme of non-thermal methane plasma of this work, the substantial methane plasma kinetic scheme presented by De Bie et al. (2011) is used as a base, and further expanded significantly by the addition of electronically and vibrationally excited species and negative ions as distinct species, and the explicit description of their reactivity. The species in the network are stated in Section 2.1. In Section 2.2 the ways that the additional species react are described.

2.1 Species considered

The kinetic scheme used considers 57 species: 38 neutral species, including molecules, metastables and free radicals, and 19 charged species, including electrons, and positively and negatively charged ions. The species used are presented in Table 1.

Table 1: Species included in the reaction network.

Molecules	Electronically excited molecules	Vibrationally excited molecules	Radicals	Positively charged species	Negatively charged species
CH_4, C_2H_6, C_2H_4, C_2H_2, C_3H_8, C_3H_6, H_2	$CH_4^*(7.9eV)$, $C_2H_4^*(3.8eV)$, $C_2H_4^*(5.0eV)$, $C_2H_2^*(1.9eV)$, $C_2H_2^*(5.1eV)$	$H_2\nu(1)$, $H_2\nu(2)$, $H_2\nu(3)$, $CH_4(\nu2,4)$, $CH_4(\nu1,3)$, $C_2H_2(\nu5)$, $C_2H_2(\nu2)$, $C_2H_2(\nu3,1)$, $C_2H_4(\nu1)$, $C_2H_4(\nu2)$, $C_2H_6(\nu1,3)$, $C_2H_6(\nu2,4)$, $C_3H_6(\nu1)$, $C_3H_8(\nu1)$, $C_3H_8(\nu2)$	CH_3, CH_2, CH, C, C_2H_5, C_2H_3, C_2H, C_2, C_3H_7, C_3H_5, H	CH_5^+, CH_4^+, CH_3^+, CH_2^+, CH^+, C^+, $C_2H_6^+$, $C_2H_5^+$, $C_2H_4^+$, $C_2H_3^+$, $C_2H_2^+$, C_2H^+, C_2^+, H_3^+, H_2^+, H^+	H^-, CH_2^-, e^-

The set of molecules included consists of CH_4, H_2 and the C_2 and C_3 hydrocarbons, which have all been observed experimentally (Puliyalil et al., 2018, Scapinello et al., 2017). The radicals and positive ions included follow from the selected molecules. The choice of vibrationally excited species considered was based on the availability of the cross sections data in the literature, sourced from the LXCAT database. The model includes some lumping of vibrational modes, in cases where the excitation energy is close ($CH_4(\nu2,4)$, $CH_4(\nu1,3)$, $C_2H_2(\nu3,1)$, $C_2H_6(\nu2,4)$, $C_2H_6(\nu1,3)$). We model $CH_4(\nu1,3)$ based on the available cross sections, but in principle on the same energy level lie also species within the P_2 polyad. For the case of hydrogen, which has only one vibrational mode, we account for

the first 3 vibrational levels ($H_2\nu(1)$, $H_2\nu(2)$, $H_2\nu(3)$). Two negative ions, those with published electron attachment cross sections, $H^-$and CH_2^-, are included as they were found to represent 3% of the overall population of the ions in the work of Gogolides et al. (1994). The electronically excited states included in the network are those with available electron impact cross section data, and whose excitation energy is lower than the threshold for dissociation by electron impact. Electronically excited states with an excitation energy above the dissociation level are assumed to dissociate instantaneously (Fridman, 2008) and were, thus, not considered in the present model. Rotationally excited species are neglected in this model on account of their low internal energy, with the assumption made that they can be treated as the equivalent ground state, in line with previous works (Farouk et al., 2008, Herrebout et al., 2002).

2.2 Reactive processes

The reaction network developed and used in this work comprises of more than 1000 reactive and relaxation processes. A full list of the reactions considered, their rate coefficients, and sources is presented in the Supplementary material (parts 1-5). The electron-neutral collisions considered, of momentum transfer, ionization, dissociation, excitation, and attachment type, have rate constants, which are dependent on the electron energy distribution function (EEDF) calculated by the BOLSIG+ electron Boltzmann equation solver (Pitchford et al., 1998), with the cross sections used retrieved from the literature, or computed, as stated in the Supplementary material (part 1). The electron-ion collisions taken into account are of dissociative recombination type, with their rates dependent on electron temperature (see Supplementary material, part 2). Despite the overall low densities of ions, these electron-consuming reactions impact on the population of radicals at short time-scales. The neutral-neutral reactions comprise the recombination of radicals, dehydrogenation, and coupling reactions, typically encountered and studied in combustion literature. The three-body reactions use pressure dependent rate constants that are parameterised following the Troe formalism, adjusted with a collision efficiency that depends on the nature of the 3^{rd} body and is higher or lower than 1 depending on how effective this 3^{rd} body is as a colliding partner (details in Supplementary material part 3).

2.2.1 Reactivity of vibrationally excited species

Due to the lack of experimental data on the reactivity of methane vibrationally excited species, a qualitative approach was adopted during modelling, according to earlier work on CO_2 dissociation plasma kinetics (Kozák and Bogaerts, 2014). Ionisation from vibrationally excited species by electron impact is treated as ionisation from the corresponding ground state. Dissociation from vibrationally excited states by electron impact is also treated as the ground state is, except, the ground state cross sections are shifted by the vibrational energy in the direction of low energy. The rate coefficients of elementary chemical reactions involving vibrationally excited states, $k_R(E_\nu, T_0)$, are

estimated using the Fridman-Macheret formula (Fridman, 2008):

$$k_R(E_\nu, T_0) = k_{R0}\, exp(-\frac{E_a - \alpha E_\nu}{RT_0})\, \theta(E_a - \alpha E_\nu) \quad (1)$$

where α is a coefficient of efficiency of the excitation energy in overcoming the activation barrier (see Supplementary material part 3 for more details), and $\theta(E_a - \alpha E_\nu)$ is the Heaviside function.

Three types of processes are included through which vibrationally excited species lose or reduce their vibrational energy: i. Transfer of vibrational energy into translational energy (bulk gas heating) by collision with other neutral species (so called VT processes); ii. Transfer of vibrational energy to other types of vibrational energy by impact with other neutral species (so called VV processes); and iii. super-elastic electron collisions.

For the VT processes, there is a release of the internal energy of the vibrationally excited species, which is converted to translational energy; no chemical bonds are broken during this type of process (although the resulting bulk gas heating might be able to induce follow-on thermal chemical reactions). VT processes occur as a vibrationally excited species, A, collides with any other particle, M, according to:

$$A_\nu + M \rightarrow A_g + M$$

where subscripts ν and g indicate vibrationally excited and ground state species, respectively. The colliding partner, M, is taken to be any of the stable molecules, as they are the most populated species. Similar processes are included for each of the vibrationally excited species included in the model.

Experimentally measured rate constants for all the considered low-energy vibrational states are taken from Starikovskiy and Aleksandrov (2013) for $CH_4(\nu 2,4)/CH_4$, $C_3H_8(\nu 1)/C_3H_8$ and $C_3H_6(\nu 1)/C_3H_6$, Heijkers et al. (2020) for $H_2\nu(1)/H_2$, Wang and Springer (1973) for $C_2H_4(\nu 1)/C_2H_4$ and $C_2H_2(\nu 5)/C_2H_2$, and Hill and Winter (1968) for $C_2H_6(\nu 2,4)/C_2H_6$. Data on methane relaxation induced by products are taken for $CH_4(\nu 2,4)/C_2H_6$ from De Vasconcelos (1976) and for $CH_4(\nu 2,4)/H_2$ from Menard-Bourcin et al. (2005). When relaxation times are available instead of rate constants, these are transformed into a pseudo-first order rate constant as explained in more detail in the Supplementary material (part 5). For processes for which no experimental results are found, the rate constants for the VT processes are estimated as suggested by Fridman (2008), using a formula proposed by Lifshitz (1974) in units of cm^{-3} mol^{-1} s^{-1}:

$$k_{VT}^{10} = 3.03 \times 10^6 (\Theta)^{2.66} m_{ij}^{2.06} exp(-0.492(\Theta)^{0.681} m_{ij}^{0.302} T_0^{-1/3}) \quad (2)$$

For the VV processes, transitions among particles with the same chemical formula were accounted for, as:

$$A_{\nu,n} + A_{\nu,m-1} \rightarrow A_{\nu,n-1} + A_{\nu,m}$$

where the subscript n corresponds with the mode number of the vibrational state of one reactant, and the subscript m indicates the mode number of the vibrational state for the other reactant. Similar formalism is adopted for the different levels $\nu(1), \nu(2), \nu(3)$ of the unique vibrational mode of molecular hydrogen. Rate constants for these processes were estimated using collision theory and transition probabilities as:

$$k_{m-1\rightarrow m}^{n\rightarrow n-1} = 4\pi\ r_A^2 P_{m-1\rightarrow m}^{n\rightarrow n-1}\sqrt{\frac{16k_B T_0}{\pi M_A}} \tag{3}$$

where $P_{m-1\rightarrow m}^{n\rightarrow n-1}$ are the probabilities of the transitions retrieved from various sources in the literature (see Supplementary material part 5 for details). Super-elastic electron collisions are treated using detailed balancing calculated with BOLSIG+ (Hagelaar and Pitchford, 2005), with the cross sections described in the Supplementary material (part 5).

2.2.2 Reactivity of electronically excited species

The reactivity of electronically excited species is also treated similarly to earlier work on CO_2 dissociation plasma kinetics (Kozák and Bogaerts, 2014). Electronically excited species have the same gas phase chemistry as their corresponding ground states. In the case of ionisation and dissociation by electron impact, electronically excited species are treated as the corresponding ground state species are, except with the ground state cross sections shifted in the direction of low energy by the excitation energy. Charge exchange reactions are the same as with the corresponding ground states.

Unlike, though, the earlier work on CO_2 dissociation plasma kinetics (Kozák and Bogaerts, 2014), all of the electronically excited states are assumed to be radiative. All of the electronically excited states containing more internal energy than the carbon-hydrogen covalent bond, 4.5 eV, ($C_2H_2^*(5.1eV)$, $C_2H_4^*(5.0eV)$, $CH_4^*(7.9eV)$) self or pre-dissociate. This type of reaction has been identified in the case of methane (Song et al., 2015), and is assumed here to also proceed in a similar manner for other electronically excited carbon-hydrogen molecules. The same rate coefficient for all the relevant cases was used, taken from van Dishoeck and Black (1988).

3 Modelling

The zero-dimensional flow reactor model, and the one-dimensional plasma fluid model, which are used in combination in this work, are described in this section. The one-dimensional model is described in Section 3.1, with details on the transport coefficients used elaborated in Section 3.2. In Section 3.3 the zero-dimensional model is presented.

3.1 The one-dimensional model

The one-dimensional model used in this work is regular and well known (Bai et al., 2019, Bleecker et al., 2003, Braun et al., 1992, De Bie et al., 2011, Gogolides et al., 1994, Herrebout et al., 2001, Koelman et al., 2017), with the implemented geometry following the design of commonly studied experimental DBD reactors (De Bie et al., 2015, 2011, Nozaki and Okazaki, 2013, Scapinello et al., 2017). In cylindrical coordinates, the calculation domain for the plasma and gas phase has $R_g \leq r \leq R_d$, while for the dielectric it has $R_d \leq r \leq R_e$ with R_g=1.1 cm, R_d=1.3 cm, and R_e=1.45 cm. A schematic of the domain is presented in Figure 1.

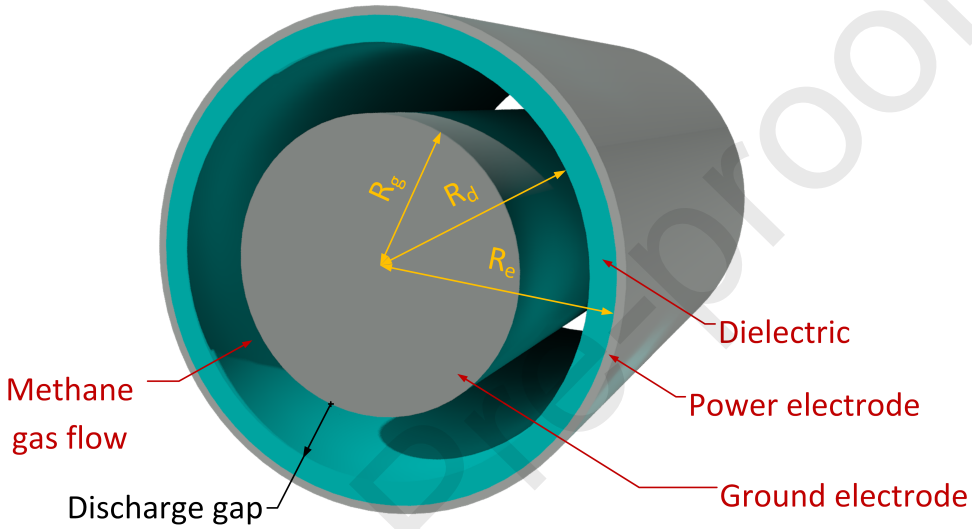

Figure 1: Schematic of the dielectric barrier discharge flow reactor defining the computational domain of the one-dimensional model.

The system of differential equations used comprises species and electron density continuity equations. For species this reads:

$$\frac{\partial n_p}{\partial t} + \vec{\nabla} \cdot \vec{j}_p = S_p \tag{4}$$

where S_p is the net rate of production of species and is calculated as:

$$S_p = \sum_r c_{p,r} r_r \tag{5}$$

in which $c_{p,r}$ is the net stoichiometric coefficient of species p in reaction r with rate r_r.

The density of the transport flux estimation is based on the drift-diffusion approximation and reads:

$$\vec{j}_\alpha = -D_\alpha \vec{\nabla} n_\alpha \pm n_\alpha \mu_\alpha \vec{\nabla} \varphi \tag{6}$$

$$\vec{j}_e = -D_e \vec{\nabla} n_e + n_e \mu_e \vec{\nabla} \varphi \tag{7}$$

208

$$\overrightarrow{j}_{\beta} = -D_{\beta}\overrightarrow{\nabla} n_{\beta} \tag{8}$$

209 The subscripts α, e, β refer to ions (positive and negative), electrons and neutrally charged species, respectively.
210 In Eq (6)-(8), the first right hand side term corresponds to diffusion, which depends on the density gradient of the
211 species and the diffusion coefficient D (see Section 3.2). The second term is the drift component, which affects
212 only the charged species and is driven by the gradient of the electric potential φ and the mobility coefficient of the
213 species μ (see Section 3.2). The charge of the ion determines the sign of the drift term (+ (-) for negative (positive)
214 ions).

215 The electron energy density is defined as $n_{\varepsilon} = \varepsilon n_e$, where ε is the local average electron energy. Similar to the
216 species continuity equations, the electron energy balance reads:

$$\frac{\partial n_{\varepsilon}}{\partial t} + \overrightarrow{\nabla} \cdot \overrightarrow{j}_{\varepsilon} = S_{\varepsilon} \tag{9}$$

217 where the effective source term of the electron S_{ε} is obtained from:

$$S_{\varepsilon} = \overrightarrow{j}_{e} \cdot \overrightarrow{E} - \sum_{r} U_{th,r} r_r - L_{elast} \tag{10}$$

218 The first term on the right-hand side above corresponds to heating of the field, the second term to the energy
219 lost in inelastic collisions (namely ionisation, excitation, dissociation, etc), and the third to elastic collisions energy
220 dissipation in the gas phase.

221 The energy density flux $\overrightarrow{j}_{\varepsilon}$ is obtained from:

$$\overrightarrow{j}_{\varepsilon} = \frac{5}{3} n_{\varepsilon} \mu_e \overrightarrow{E} - \frac{5}{3} D_e \overrightarrow{\nabla} n_{\varepsilon} \tag{11}$$

222 The electron temperature in K (used for the calculation of electron-ion recombination rates) is obtained from
223 the electron energy via $T_e = \frac{2}{3}\frac{\varepsilon}{k_B}$.

224 Finally, the balance of the charges and the field distribution are calculated using Poisson's equation:

$$\varepsilon_0 \nabla^2 \varphi = -\mathrm{q}(\mathrm{n}_{\alpha^+} - \mathrm{n}_{\mathrm{e}} - \mathrm{n}_{\alpha^-}) \tag{12}$$

225 Inside the dielectric this equation becomes $\varepsilon_0 \nabla^2 \varphi = 0$.

226 The boundary conditions are sticking and reflection of species to the walls based on individual species sticking
227 coefficients; secondary electron emission; surface charge accumulation; and values of applied potential:

228 at $\boldsymbol{r} = R_g$:

$$\varphi = 0 \tag{13}$$

$$\overrightarrow{j}_{\alpha,\beta} \cdot \overrightarrow{n} = s_{\alpha,\beta} n_{\alpha,\beta} (a\mu_{\alpha,\beta} \overrightarrow{E} \cdot \overrightarrow{n} + \frac{1}{4} v_{th,\alpha,\beta}) \tag{14}$$

$$\overrightarrow{j}_{e} \cdot \overrightarrow{n} = s_s n_e (a\mu_e \overrightarrow{E} \cdot \overrightarrow{n} + \frac{1}{4} v_{th,e}) - \gamma \sum \overrightarrow{j}_{\alpha^+} \cdot \overrightarrow{n} \tag{15}$$

at $\boldsymbol{r} = R_d$:

$$\rho = \varepsilon_0 \varepsilon_r \overrightarrow{E}_{diel} \cdot \overrightarrow{n} - \varepsilon_0 \overrightarrow{E} \cdot \overrightarrow{n} \tag{16}$$

$$\overrightarrow{j}_{\alpha,\beta} \cdot \overrightarrow{n} = s_{\alpha,\beta} n_{\alpha,\beta} (a\mu_{\alpha,\beta} \overrightarrow{E} \cdot \overrightarrow{n} + \frac{1}{4} v_{th,\alpha,\beta}) \tag{17}$$

$$\overrightarrow{j}_{e} \cdot \overrightarrow{n} = s_e n_e (a\mu_e \overrightarrow{E} \cdot \overrightarrow{n} + \frac{1}{4} v_{th,e}) - \gamma \sum \overrightarrow{j}_{\alpha^+} \cdot \overrightarrow{n} \tag{18}$$

at $\boldsymbol{r} = R_e$:

$$\varphi = V_0 sin(\omega t) \tag{19}$$

where, ε_0 is the vacuum permittivity, ε_r is the relative permittivity of the dielectric that is set to 9 (-), γ is the secondary electron emission coefficient that is set to 0.001 (-). The sticking coefficients used are from Eckert et al. (Eckert et al., 2008).

This model was implemented using the commercial finite volume analysis software Plasimo (Dijk et al., 2009). Some of the results published in De Bie et al. (2011) were reproduced in order to validate the implementation of the model (not shown).

3.2 Transport coefficients

The ion mobility coefficient, $\mu_{i,j}$, (m^2 V^{-1} s^{-1}) of an ion j in background gas i is calculated using the low electric field Langevin mobility expression:

$$\mu_{i,j} = 0.515 \frac{T_0}{p\sqrt{m_{ij}\alpha_i}} \tag{20}$$

where α_i is the polarizability of the background gas (using a value of 2.6 $Å^3$ for methane from Böttcher (1973).

The diffusion coefficient, D_{ij}, (m^2 s^{-1}) of neutral species j in background gas i is obtained by the Chapman-Enskog equation:

$$D_{ij} = \frac{3k_B T_0 \sqrt{\frac{4\pi k_B T_0}{2m_{ij}}}}{16 p \pi \sigma_{ij}^2 \Omega_D(\Psi)} \tag{21}$$

where Ω_D is the dimensionless diffusion collision integral. This collision integral, which is a function of the dimensionless temperature Ψ, is given by:

$$\Omega_D(\Psi) = \frac{A}{\Psi^B} + \frac{C}{e^{D\Psi}} + \frac{E}{e^{F\Psi}} + \frac{G}{e^{H\Psi}} \tag{22}$$

where Ψ equals $\frac{k_B T_0}{\varepsilon_{ij}}$, $A = 1.06036$, $B = 0.15610$, $C = 0.19300$, $D = 0.47635$, $E = 1.03587$, $F = 1.52996$, $G = 1.76474$, and $H = 3.89411$ (De Bie et al., 2011). σ_{ij} and ε_{ij}, being the characteristic length and energy for

every species in the 12-6 Lennard–Jones potential (taken from Gao et al. (2016), are calculated by $\sigma_{ij} = \frac{\sigma_i+\sigma_j}{2}$ and $\varepsilon_{ij}=\sqrt{\varepsilon_i\varepsilon_j}$ with ε in units of J. The background gas is assumed to be pure methane. Further details are provided in the Supplementary material (part 6)

3.3 The zero-dimensional model

The previously presented 1D model allows the accurate description of plasma features such as streamer propagation and field breakdown, however its combination with the very complex chemistry implemented in this work renders the execution of simulations longer than a few ms very expensive computationally and practically non feasible. Global models (also known as zero-dimensional) cannot describe the spatial variation of discharges, but enable the simulation of much longer time scales, much greater than the characteristic times of electron dynamics (Maitre et al., 2020), and closer to the residence time of laboratory reactors typically used for studying kinetics

For this purpose, a zero-dimensional flow reactor model is also developed in this work, whose output, though, is based on input from the 1D model. Terms describing flows into and out of the reactor, and losses of species to the walls, are taken into account in line with Hurlbatt et al. (2017). The following ordinary differential equations are solved:

$$\frac{dn_\alpha}{dt} = r_\alpha(\frac{E}{N}, T_0, T_e) - \frac{A}{V}\sqrt{\frac{k_B T_e}{M_\alpha}}n_\alpha - \frac{n_\alpha}{\tau} \tag{23}$$

$$\frac{dn_\beta}{dt} = r_\beta(\frac{E}{N}, T_0, T_e) - s_\beta\frac{A}{V}\sqrt{\frac{3k_B T_0}{M_\beta}}n_\beta - \frac{n_\beta}{\tau} + \frac{n_{\beta_0}}{\tau} + L_{reflection} \tag{24}$$

The rate and transport coefficients used are the same as in the one-dimensional model. The radially averaged electron density, and the radially averaged electric field, for one period (which is repeated for the duration of each simulation), are obtained from the one-dimensional model and used as inputs in the zero-dimensional reactor model (see Section 4.1 for details). This method enhances the accuracy of the 0D model, which typically cannot account for charge spatial diffusion and accumulation (e.g. at the dielectric), as the electron density and the field values used have been calculated in a self-consistent manner in the 1D model. The second term on the right hand side of Eq. (23)-(24) describes fluxes of species lost to the walls. The velocity of the flux is estimated as the thermal velocity for neutral species. The velocity of the flux of ions lost to the walls is estimated as the Bohm velocity. The third term on the right hand side of Eq. (23)-(24) describes the flow of the mixture out of the vessel. The fourth term on the right hand side of Eq. (24) refers to the flow of pure atmospheric pressure methane into the reactor, and equals zero for all other species. Finally, the term $L_{reflection}$ describes the reflection back into the discharge of ground state neutrals that were electronically excited on collision with the vessel walls and is calculated via Eq. (25), with $\beta*$ denoting the electronically excited states.

$$L_{reflection} = s_{\beta*}\frac{A}{V}\sqrt{\frac{3k_BT_0}{M_{\beta*}}}n_{\beta*} \tag{25}$$

The sticking coefficients, s, used for the short time-scale simulations (Section 4.1) are the same as in the one-dimensional model. For the long time-scale flow reactor simulations (Section 4.2) use of these sticking coefficient values resulted in unrealistically high carbon losses to the walls, which is in line with observations of similar studies under equivalent assumptions (De Bie et al., 2011). For such long time scales, for a fully consistent model to be developed, a carbon deposition model should be incorporated, along the lines of previous works (Bera et al., 2001, Farouk et al., 2008, Pourali and Foroutan, 2015, Yarin et al., 2006), however this was out of the scope of the present study. Results are presented primarily from simulations where the sticking coefficients of the least mobile radicals (carbon number of 2 and higher) were set to zero, while keeping the rest (ions, smaller radicals) at their literature values, however in the Supplementary material the impact of these sticking coefficients on carbon balance closure is further investigated (part 7). The geometry of the reactor vessel simulated is the same as in the one-dimensional model. The zero-dimensional model is implemented using the ZDPlasKin solver (Pancheshnyi et al., 2008).

4 Results and discussion

4.1 Short time-scale dielectric barrier discharge modelling

Modelling is performed of a dielectric barrier discharge in pure atmospheric pressure methane, with an applied sinusoidal voltage of 8 kV amplitude and 25 kHz frequency, for 0.2 ms, using the one-dimensional dielectric barrier discharge model.

As shown in Figure 2, the radially averaged electron density peaks periodically, preceded by peaks in the reduced field, under the applied sinusoidally varying voltage. This peaking corresponds with the process of streamer and then micro discharge formation. With an increasing maximum of the applied voltage, each time period would have more peaks of electron density. Generally, with increasing frequency, the number of electron density peaks per voltage period remains the same. Indicative results on the effect of applied voltage and frequency on the reduced field and the electron density are presented and further discussed in the Supplementary material (part 8).

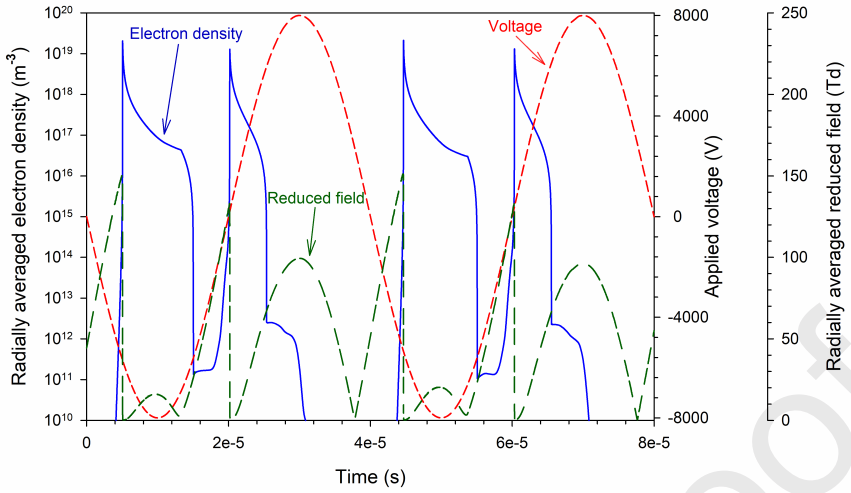

Figure 2: Radially averaged electron density (left axis), voltage (first right axis), and radially averaged reduced field (second right axis) vs. time. The voltage amplitude is 8 kV and the frequency is 25 kHz.

The radially averaged loss terms of the most important processes for the electron energy density continuity equation during a period are plotted in Figure 3. It can be seen that, across the whole period, the energy lost towards the vibrational excitation of methane is overall dominant. This agrees well with previous studies (Gao et al., 2018, Sun and Chen, 2019) having reported the energy lost towards excitation channels of methane to be two orders of magnitude higher than the energy lost in elastic collisions. Nonetheless, close to the most energetic peak of electrons, the electronical excitation of methane and its first and second dissociations ($e^- + CH_4 \rightarrow CH_3 + H + e^-$ and $e^- + CH_4 \rightarrow CH_2 + H_2 + e^-$) become more prominent (see Figure 3(b)). This is due to the higher reduced field that is reached during that short period of time that allows processes with higher energy thresholds to occur more efficiently. It is finally interesting to point out that the first ionization and first dissociative ionization of methane ($e^- + CH_4 \rightarrow CH_4^+ + 2e^-$ and $e^- + CH_4 \rightarrow CH_3^+ + H + 2e^-$), even though necessary to sustain the plasma, are always the lowest energy consuming processes on account of their higher energy thresholds. Across the period, they are found to consume two orders of magnitude less energy or even lower than that in comparison to other processes.

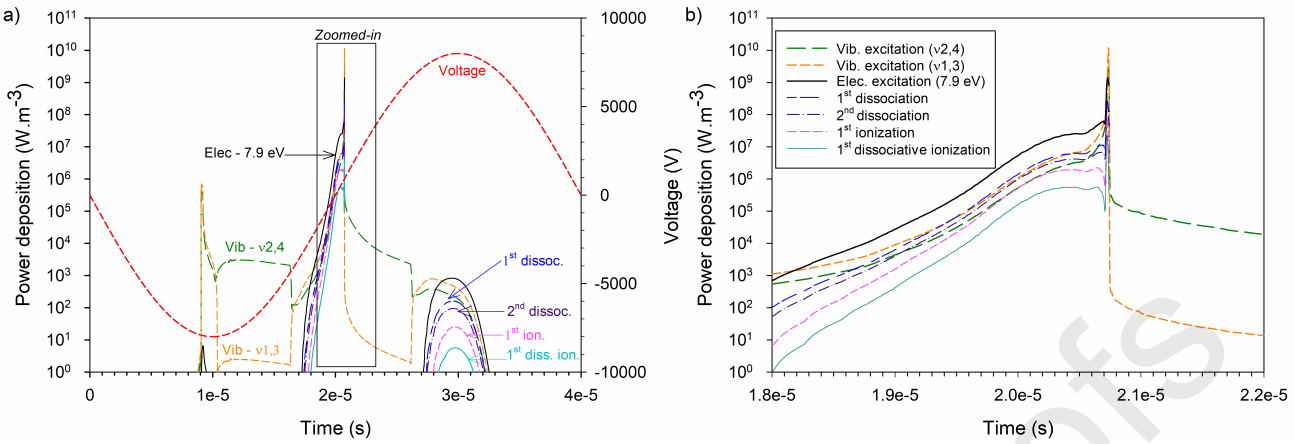

Figure 3: (a) Radially averaged power consumption from most important electron impact processes vs. time during a voltage period (8 kV, 25 kHz), (b) close-up on the most energetic peak.

The time averaged densities over one voltage period across the discharge gap for the short-lived species, presented in Figure 4, are seen to span across a very broad range. The densities of electrons and positive ions are approximately equal, as generally observed in electro-positive plasmas such as of methane (De Bie et al., 2011, Fridman, 2008, Gogolides et al., 1994, Tachibana et al., 1984), and in magnitude very close to previously reported values (De Bie et al., 2011, Nozaki et al., 2004, Puliyalil et al., 2018). The slightly higher density of ions at the side of the dielectric is typical for the sheath region of a plasma and is a manifestation of the large difference in masses between the electrons and the ions, that leads the former to escape from the plasma towards the walls at much higher velocities. The density of negative ions is close to four orders of magnitude lower than the positive ones, as expected for an electro-positive plasma. For an RF methane plasma at 1 Torr a ratio between positive and negative ions densities of about 30 was reported by Gogolides et al. (1994), however in the current work the higher pressure applied promotes effectively the ion-neutral reactions below and results in a net consumption of negative ions:

$$H^- + CH_4 \rightarrow H + e^- + CH_4$$

$$CH_2^- + CH_4 \rightarrow CH_2 + e^- + CH_4$$

The very different orders of magnitude of the excited species densities should also be noted. Whereas the vibrationally excited species are 10^2 to 10^3 times less populous in comparison to the background gas ($\approx 2.45 \times 10^{25}\, m^{-3}$), the electronically excited species are on average 10 orders of magnitude less populated due to their high internal energy that drives their self-deexcitation by emission of a photon or by self-dissociation.

Finally, the formation of a sheath is visible in the profiles of all species at both sides of the discharge gap, with the higher electron energy in that region resulting in enhanced reactivity and species creation.

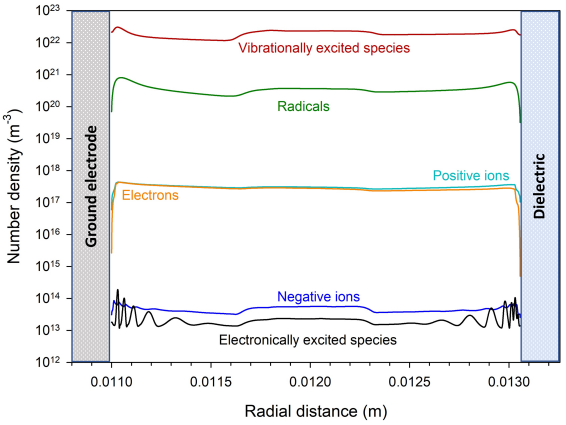

Figure 4: Radial density profiles of different types of short-lived species, time averaged over a voltage period.

As discussed by Bogaerts et al. (2019), the incorporation of detailed plasma chemistry in high dimensionality fluid models is very demanding in terms of computational cost, prompting researchers to develop different methods to overcome this issue. De Bie et al. (2011) used the time averaged electron density, electron energy and electron impact rate coefficients from a 1D model as input in a global model, with the terms being updated from the fluid model as needed, while Moss et al. (2017) investigated the splitting of CO_2 in a corona discharge by solving a 1D model over a short period of time to obtain the periodic electron density and rates of electron processes, further used in a 0D solver for longer time scale simulations. More recently, the formation of microdischarges in DBD was modelled through sub-sequences of pulses followed by afterglow periods alternating spatially within one (Toth et al., 2018) or multiple in series (Molteni and Donazzi, 2020) 1D steady state plug flow reactor instead of temporally within a 0D transient perfectly mixed reactor. Closer to the approach by Moss et al., in this work the radially averaged electron density, and radially averaged reduced electric field, as shown in Figure 2, are both used as input into the zero-dimensional model for a combined modelling approach. A comparison between the one-dimensional DBD modelling and the zero-dimensional reactor modelling is presented in Figure 5. It can be seen that for this short initial period of time there is a good qualitative agreement between example ion, radical, and excited species densities. Quantitatively the agreement can differ by maximum an order of magnitude. The findings from the combined zero-dimensional and one-dimensional modelling approach over long time periods presented in the following should be understood primarily as of qualitative accuracy, nonetheless allowing to probe the behaviour of the system at time scales prohibitive to the one-dimensional approach.

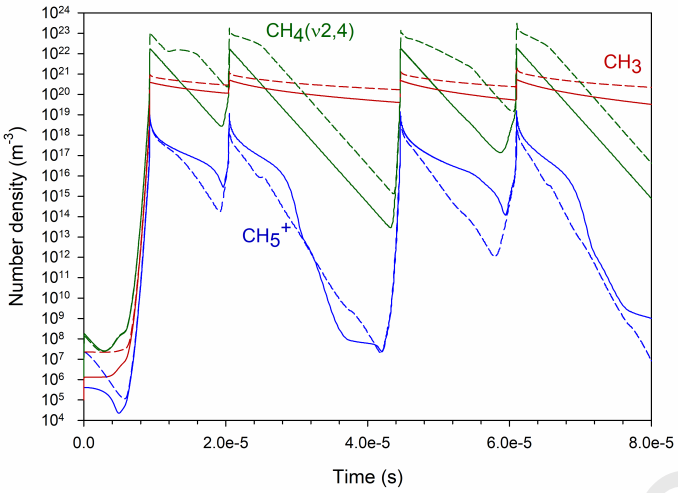

Figure 5: Comparison of CH_3, $CH_4\,(\nu 2, 4)$, and CH_5^+ densities from the one-dimensional model (solid lines) and the combined one-dimensional and zero-dimensional modelling approach (dashed lines). The voltage amplitude is 8 kV, the frequency is 25 kHz.

4.2 Long time-scale reactor modelling

Simulations are performed of a characteristic experimental methane upgrading dielectric barrier discharge flow reactor, with an applied voltage of 8 kV amplitude and 25 kHz frequency, as above. Various reactor residence times are simulated, in each case up to the time where the reactor reaches a quasi steady state, with conversion remaining essentially constant with further increase of time (typically achieved after about 5 times the equivalent residence time τ). The specific energy density input (SEI), originating from the energy channeled in the plasma by the electrons, varies as the residence time is varied. It is calculated by integrating the power density, P_d, across the residence time, with the power density obtained from:

$$P_d = q n_e v_e \frac{E}{N} \tag{26}$$

n_e and $\frac{E}{N}$ are the radially averaged repeated values from the one-dimensional simulations, while v_e is calculated during the simulations by BOLSIG+. The specific energy density input is estimated by dividing the integral of P_d across the whole simulation time (5τ) by 5. Reactor residence times are varied between 0.001 s and 0.5 s in order to cover the range of specific energy density inputs of relevant literature experimental results used for the validation of the model. The residence times studied are lower to typical experimental values, which range in the order of seconds, due to the homogeneous nature of the implemented 1D and 0D models that do not account for the filamentary behaviour of DBD plasma. Nonetheless, as the energy density input is respected, the comparison with experiments is considered valid. The conversion of methane at various residence times and the equivalent SEI

obtained are presented in Table 2. The conversion of methane, X_{CH_4}, was calculated as:

$$X_{CH_4} = \frac{n_{CH_4 feed} - n_{CH_4 lump}}{n_{CH_4 feed}} \tag{27}$$

where, $n_{CH_4 feed}$, is the methane density in the feed gas and $n_{CH_4 lump}$ is the sum of the reactor densities of the ground state methane and all of its excited states:

$$n_{CH_4 lump} = n_{CH_4} + n_{CH_4(\nu 2,4)} + n_{CH_4(\nu 1,3)} + n_{CH_4^*(7.9eV)} \tag{28}$$

Table 2: Methane conversion at quasi steady state and specific energy density inputs for various reactor residence times obtained using the zero-dimensional model

Residence time (s)	SEI (MJ/m^3)	Methane conversion (%)
0.001	0.636	0.271
0.01	6.302	2.465
0.025	15.94	5.319
0.050	32.44	9.007
0.1	62.96	14.20
0.2	130.6	21.45
0.3	194.8	27.37
0.4	259.6	32.70
0.5	324.5	37.11

The conversion values obtained from the model are compared against literature experimental conversion data in Figure 6 and found to be in good quantitative agreement for the whole range of the energy density inputs studied. In all these experiments an approximately equivalent reactor geometry was applied, as in the present simulations, with similar electrode gap and applied voltage (thus also field), while the feed gas was also pure methane at atmospheric pressure.

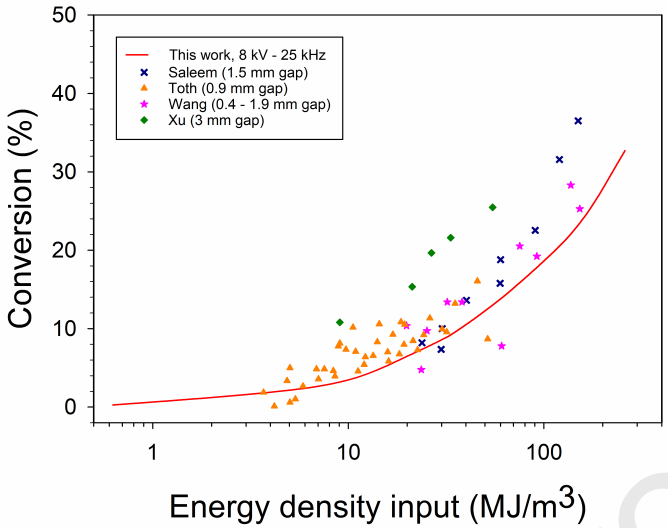

Figure 6: Comparison of methane conversion simulation results and experimental data from Saleem et al. (2019), Xu and Tu (2013), Wang et al. (2013), Toth et al. (2018).

In order to investigate the conversion channels of methane, we further consider the selectivities and carbon balance. The individual carbon-based product selectivities, $S_{C_xH_y}$, are calculated as follows:

$$S_{C_xH_y} = \frac{x n_{C_xH_y}}{n_{CH_4 feed} - n_{CH_4 lump}} \tag{29}$$

where $n_{C_xH_y}$ refers to the density of any carbon containing species (molecules, radicals, ions), while for molecules that exist in different excited states a density lump $n_{C_xH_y(lump)}$ is considered similar to the case of methane. The carbon balance, $C_{balance}(\%)$, describes the percentage of methane converted to gas phase species and allows determining the carbon fraction lost to the walls. It is calculated as:

$$C_{balance} = \sum_{i=1}^{n_{products}} S_{iC_xH_y} \tag{30}$$

The selectivities towards the stable hydrocarbon products in function of the methane conversion and the energy input are presented in Figure 7. Ethane is the primary product, evident from its selectivity trend approaching a finite value as the conversion of methane tends to zero. At higher conversions and energy inputs, ethylene and acetylene selectivities increase at the concurrent decrease in ethane's selectivity indicative of the progressive dehydrogenation of the C_2 species. These general trends are consistent with observations from relevant literature. As reviewed e.g. in Scapinello et al. (2017), experimentally it has also been widely observed that the selectivity towards ethane decreases at higher energy inputs due to the latter's dehydrogenation. Noticeably, though, the predicted selectivity of acetylene reaches values at the higher conversions simulated, not commonly reported in

DBD experimental studies, where ethane remains typically the most abundant product independent of energy input (Saleem et al., 2019, Wang et al., 2013, Xu and Tu, 2013). Nonetheless, in the modelling work of Yang (2003b) methane conversion was seen to be progressively channeled from ethane to acetylene formation depending on energy input, although the transition was predicted to occur at rather high energy input values (90 eV/molecule $\approx$ 350 MJ/m^3). In De Bie et al. (2011) ethane was identified as the main product at low methane conversion (<10%) with acetylene becoming again the dominant one further on. The overprediction of acetylene in contrast to experimental literature was attributed by the authors to the possible lack of polymerization pathways in the kinetic network, which holds also for the current work. It is further to be noted that acetylene is indeed a dominant product in more homogeneous high energy discharges (Dors et al., 2014, Fincke et al., 2002, Indarto et al., 2005, Yao et al., 2002), which could indicate that the homogeneous nature of the discharge simulated further impacts the dehydrogenation pathways in our model.

The highly varied experimental configurations and conditions used (temperature, gap length, etc.) and their many times opposing effects on selectivities makes a quantitative comparison with the present results challenging. Indicatively, Wang et al. (2013) reported a lumped selectivity towards C_2 hydrocarbons between 54% and 72%, Xu and Tu (2013) between 51% and 58% and Saleem et al. (2019) between 30% and 41% . The C_2 selectivity lump from the model remains approximately at 90% across the whole range of conversions studied (Figure 7) implying that further creation channels towards higher hydrocarbons species need to be possibly considered or that nonidealities within the experimental systems are not captured by the current zero-dimensional model. Similar underprediction of C_3 hydrocarbons was reported also in prior simulation works for RF (Sun and Chen, 2019) and DBD (Heijkers et al., 2020) discharges, underlining the need for these effects to be more rigorously accounted for.

The sticking of radicals to the reactor walls was also observed to have a significant impact on the obtained conversion and selectivities. As discussed, results presented in this section were obtained by setting the sticking coefficients of the least mobile radicals (carbon number of 2 and higher) to zero, however additional cases were investigated with respective results shown in the Supplementary material (part 7). Using for all radicals the same sticking coefficients as those from the 1D model during the long time scale simulations, an agreement with experimental conversion data similar to that of Figure 6 was obtained. However, significant losses of selectivity up to 70% of the total carbon balance were observed due to the sticking of C_2H_3, C_2H_5 and C_2H radicals to the walls. On the contrary, when sticking for all species was not considered, no carbon losses were obviously observed, however much lower conversions were predicted, in large disagreement with the experimental data. For the latter simulation scenario, the much more populous H radicals, not getting lost to the walls anymore, appeared to promote the re-hydrogenation of CH_3 leading to an overall drop in conversion, unlike thermal plasma discharges (Li et al., 2004, Scapinello et al., 2019), where H radical-mediated hydrogen abstraction has been observed to promote methane conversion. In the experimental studies used for comparison in this work (Saleem et al., 2019, Wang et al., 2013, Xu and Tu, 2013), carbon losses up to 30% of the total carbon fed were reported indicating that more sophisticated

models are required to properly describe this characteristic of the system and accurately account for its impact on kinetics. As discussed above, rigorous model validation against reactor scale experimental data, particularly for spatially heterogeneous DBD that exhibit highly localized features such as filaments, would require models of high dimensionality at prohibitive computational cost. Given that in the current model, besides disabling the sticking of certain radicals on walls during long time scale simulations, no adjustable parameters have been considered, the agreement with existing experimental trends on reactors of similar geometry is considered adequate for the purposes of analyzing the kinetic pathways and the role of excited species.

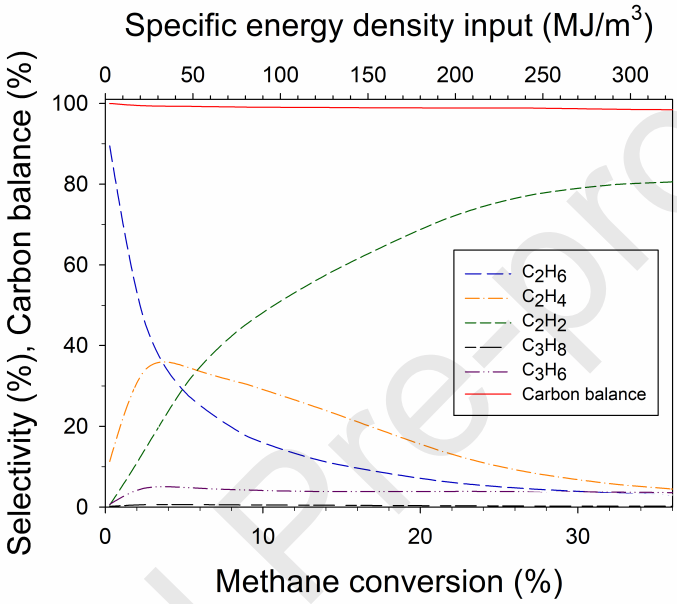

Figure 7: Carbon-based selectivities to C_2 and C_3 molecules and carbon balance towards gas phase products.

4.3 The role of excited species in methane upgrading

In Figure 8 the evolution in time of the densities of H_2, C_2H_6, CH_4, (the three most populated species of the gas phase at these conditions) and their respective excited states is shown for a reactor with residence time of 0.01 s. All the excited states of methane exhibit very transient behavior with fast production during an electron event and subsequent deexcitation (Figure 8(b)). The lower energy vibrationally excited methane state, $CH_4(\nu 2, 4)$, is the most populous, with its density seen to reach approximately 1% that of the ground state at the tip of the peak. This high density is due to the effective creation of this species via electron collisions and the deexcitation of the $CH_4(\nu 1, 3)$ state via the VV channel. At an early stage in the simulation, the depletion of $CH_4(\nu 2, 4)$ is due to its VT relaxation via the loss channel:

$$CH_4(\nu 2, 4) + CH_4 \rightarrow CH_4 + CH_4$$

Equivalent VT loss channels with products H_2 and C_2H_6, shown below, become more important as the density of these species increases over time with methane's conversion. At the simulated conditions, their rate constants

are 10 and 100 times larger to the VT channel with ground state CH_4, respectively, significantly contributing in reducing the population of $CH_4(\nu 2, 4)$ at the later stages of the simulation that the reactor has approached quasi steady state (Figure 8(b)).

$$CH_4(\nu 2, 4) + C_2H_6 \rightarrow CH_4 + C_2H_6$$

$$CH_4(\nu 2, 4) + H_2 \rightarrow CH_4 + H_2$$

$CH_4(\nu 1, 3)$ is efficiently produced during electron streamers, but rapidly deexcites (even faster than $CH_4(\nu 2, 4)$) via the VV channel

$$CH_4(\nu 1, 3) + CH_4 \rightarrow CH_4(\nu 2, 4) + CH_4(\nu 2, 4)$$

resulting in strongly oscillatory variations in its density between values of 10^2 m^{-3} and 10^{21} m^{-3} in between streamer events.

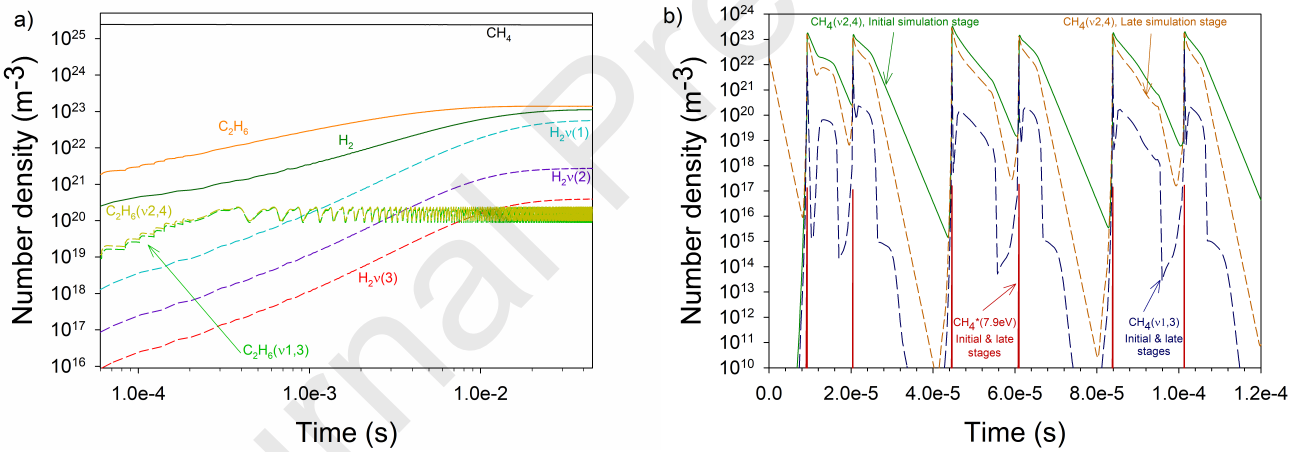

Figure 8: Evolution of CH_4, H_2, C_2H_6 and their excited states vs. time for a reactor with residence time of 0.01 s. a) Density profiles of ground states and H_2, C_2H_6 excited states across a simulation time of 5τ. b) Density profiles of CH_4 excited states at initial and late stages of simulation. For the latter case, the x-axis refers to time following a simulation time of 5τ. For $CH_4^*(7.9eV)$ and $CH_4(\nu 1, 3)$, no discernible differences exist between the two stages.

The short lifetimes of these vibrationally excited states (in the range of 0.01-0.1 ms) makes experimental validation of the predicted densities challenging. Nonetheless, the much higher density of bending modes, $CH_4(\nu 2, 4)$, compared to the stretching ones, $CH_4(\nu 1, 3)$, at any point of the cycle is consistent with previous experimental results (Butterworth et al., 2020, De Vasconcelos, 1976, Menard-Bourcin et al., 2005). In modelling studies, Nozaki and Okazaki (2013) and Sun and Chen (2019) estimated similar orders of magnitude for methane and its vibrationally excited states, however the absence of VV processes in the kinetic networks of those works resulted in modes $v2, 4$ and $v1, 3$ having equivalent densities, unlike results reported here.

The electronically excited state of methane at 7.9 eV, $CH_4^*(7.9eV)$, is much less abundant (its density exhibiting strong oscillations between 10^{-6} m^{-3} and 10^{17} m^{-3}), as is the case with other electronically excited molecules, due to their rapid predissociation or radiative deexcitation following their formation during streamer events. No significant variation is observable in the densities of $CH_4^*(7.9eV)$ and $CH_4(\nu 1,3)$ between the initial stage of the simulation and once the reactor has reached quasi steady state (Figure 8(b)), further evidencing that the respective differences for $CH_4(\nu 2,4)$ originate from its VT relaxation enhancement due to products accumulation.

The densities of the excited states of H_2 remain lower than those of the ground state, decreasing by increasing order of the excited state's internal energy. $H_2\nu(1)$ that has an internal energy of 0.5 eV higher than the ground state is the most populated, while $H_2\nu(3)$, at 1.5 eV, is the least populated. The density of $H_2\nu(1)$ approaches that of the ground state at 10^{23} m^{-3}, similar to what was observed for the lower vibrational level of CH_4 discussed above. The density trends for hydrogen and its excited modes qualitatively agree with the observations of Sun and Chen (2019), however it needs to be noted that in that work this behaviour was attributed to the consumption of the vibrational states via process $H_2\nu(2,3) + C \rightarrow CH + H$. The rate of this process was enhanced due to the high vibrational energy of these states (1.0 and 1.5 eV, respectively), as described by the Fridman-Macheret model. In the current work, this process is considered barrier-less (see Supplementary material), hence such rate enhancement is not applicable, and indicates a possible use of different kinetic source data. The increase in the densities of the vibrationally excited states based on the inverse of their internal energy is found actually to hold for largely all molecules in this work and can be attributed to a combination of factors: i. The rate coefficient for the vibrational excitation of molecules by electron impact generally decreases with increasing internal energy of the excited species. ii. With increasing internal energy of the excited species, there is an increase in the rate coefficients of endothermic gas phase reactions that these states participate at. iii. The higher energy effectively deexcites into the lower levels via VV relaxation processes. Interestingly, for C_2H_6 the excited states population is closer to each other than for methane and hydrogen, indicating that VT relaxation of $C_2H_6(\nu 2,4)$ and VV relaxation of $C_2H_6(\nu 1,3)$ proceed at equivalent rate, in qualitative agreement with the observations of Hill and Winter (1968) (quoting Valley and Legvold (1962)).

Finally, it is noted that the excitation from the lower levels to the higher levels, for example by electron impact, was not taken into account in this work, as is also typically the case for similar works in methane plasma literature. Nonetheless, in studies related to CO_2 splitting via plasma, where the description of all vibrational levels of CO_2 in detail is of primary importance due to the process concept, (Bogaerts et al., 2015, Koelman et al., 2017, Kozák and Bogaerts, 2014) cross sections for such collisions have indeed been estimated using a semi-empirical approximation suggested by Fridman (2008). In the current work only cross sections originating from published databases of, primarily, experimental data were used, hence excitations of already excited molecules were not considered.

Recent theoretical work by Nikitin et al. (2018) who calculated methane vibrational energy levels up to 10300 cm^{-1} ($\approx 1.28\,eV$) as various combinations of the 4 fundamental vibrational levels ($\nu 1 - 4$) could drive the further

extension of methane plasma kinetic models, although approaches to estimate the relevant electron impact cross sections would be needed.

In Figure 9 the percentage of the total energy spent on various processes is shown for the duration of an entire simulation of a reactor with residence time of 0.1 s. These values were calculated by integrating over time the respective rates of each process multiplied further by its threshold energy, and divided by the specific energy density input. When the conversion is very low, excitation of CH_4 accounts for almost all of the energy consumption (>90%). As conversion increases, though, and the reactor approaches a periodic steady state (after ~0.4 s), the energy fraction towards methane excitation decreases and tends towards a plateau. The dissociation by electron collisions of ground state CH_4 is seen to account for roughly 3-4% of the total energy consumption across the simulated time. The excitation of C_2H_4 and C_2H_2 become important energy consumption channels as the respective species start to accumulate in the gas bulk with rising conversion. Eventually, when the reactor has reached a quasi steady state at a conversion of 14.1%, 86% of the electron energy is spent on the excitation of the species in the reactor :

- 68.1% to CH_4 excited states (20.8% to $CH_4(v2,4)$, 34.7% to $CH_4(v1,3)$ and 12.6% to $CH_4^*(7.9eV)$)
- 12.6% to the electronically excited states of C_2H_2
- 5.1% to the electronically excited states of C_2H_4

These results are in good agreement with the work of Butterworth et al. (2020), who estimated that 50-90% of the energy is transferred into vibrational levels and 10-50% into electronical excitation and ionisation. Finally, the energy lost in collisions with radicals and C_3 products remains very low (<0.1% of the total) due to the small number densities of these species and is thus not shown on Figure 9.

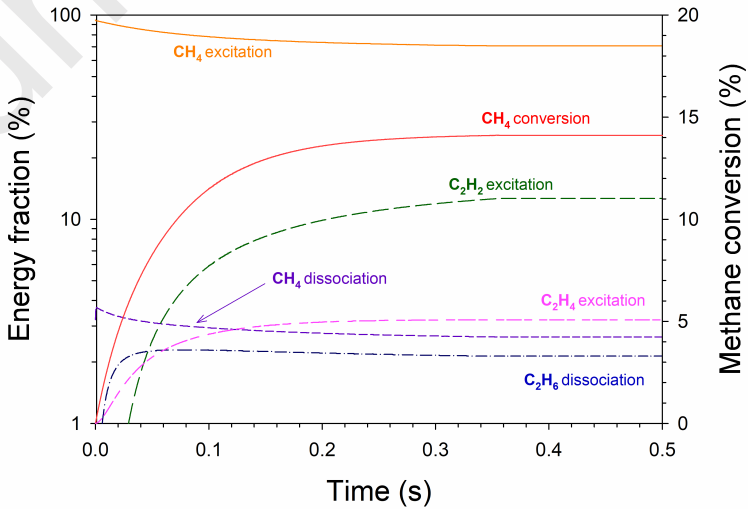

Figure 9: Energy dissipation into the various reaction channels and methane conversion vs. time for a reactor with residence time of 0.1 s.

4.4 Reaction pathway analysis

The production and consumption pathways of various species are investigated by means of a reaction pathway analysis. Several types of data are presented in the following for a complete analysis of the various time scales and differences in reactivity of the multitude of species in the plasma system. The first type of analysis is performed at a peak of electron density, for a reactor with residence time of 0.1 s that has reached quasi steady state, at a methane conversion of 14.1% (Figure 10). In this figure, the presented data refer to differential net consumption rates that are homogeneous to $m^{-3}.s^{-1}$.

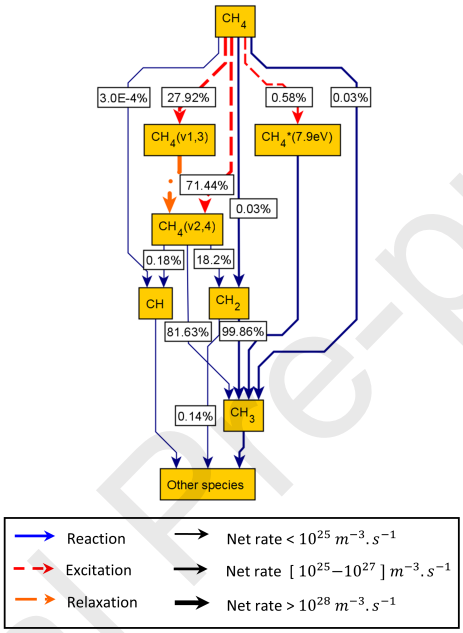

Figure 10: Differential reaction pathway analysis for CH_4. Analysis performed at a peak of electron density, for a reactor of 0.1 s residence time in quasi steady state.

Moreover, Figure 11 presents integral reaction pathway analysis results for CH_4, C_2H_6 and C_2H_4, while in Figure 12 similar integral results are presented for C_2H_2, H_2 and the overall process. In the latter case of integral data (for the overall process), lumps of molecules are considered, with excited states not distinguished from equivalent ground states. For all integral results, net rates are integrated across a period of the applied voltage for the same reactor of 0.1 s residence time at quasi steady state and are presented as net production values in m^{-3}. The thickness of the arrows indicates the magnitude of the consumption Q_i of each channel in relation to the rest, while the percentages shown refer to the net rates of consumption of each source species towards the target species.

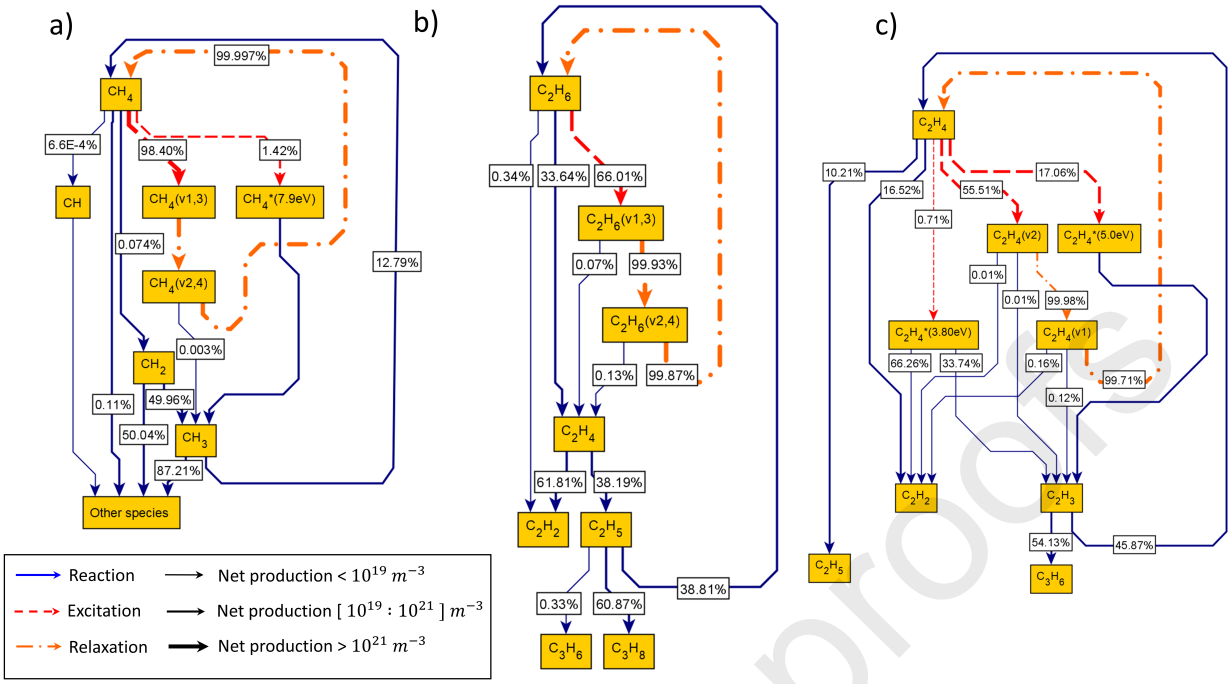

Figure 11: Integral reaction pathway analysis for (a) CH_4, (b) C_2H_6, (c) C_2H_4 across a voltage period for a reactor of 0.1 s residence time in quasi steady state.

Methane

Methane, being the feed gas, is as expected very populous. As the electron density peaks, 71.44% of ground state methane is converted into $CH_4(\nu 2,4)$, and 27.92% into $CH_4(\nu 1,3)$ (Figure 10). The creation of $CH_4(\nu 1,3)$ takes place exclusively via electron collisions with ground state CH_4, while for $CH_4(\nu 2,4)$ only 35.61% of its formation is via this route, with the very fast VV relaxation process being responsible for a substantial contribution of 64.39% to the species's creation:

$$CH_4(\nu 1,3) + CH_4 \rightarrow CH_4(\nu 2,4) + CH_4(\nu 2,4)$$

Once formed, $CH_4(\nu 2,4)$ leads to the creation of CH_3 via two channels:

$$e^- + CH_4(\nu 2,4) \rightarrow CH_3 + H + e^-$$

$$CH_4(\nu 2,4) + C_2H \rightarrow C_2H_2 + CH_3$$

with the electron collision channel and recombination reaction only accounting for 0.066% and 0.067% of the radical's formation, respectively. The analogous processes involving the ground state methane account for 9.47% and 6.03% of CH_3 formation, respectively.

The electronic excitation of ground state methane accounts for 0.58% of its conversion during the high electron energy peak (Figure 10), however the high internal energy of $CH_4^*(7.9eV)$ rapidly leads to the creation of CH_3

radicals via the predissociation reaction below. During the electron peak this process is found to be responsible for 78.81% of CH_3 radicals creation:

$$CH_4^*(7.9eV) \rightarrow CH_3 + H$$

Figure 11(a), presenting the integral RPA results for CH_4 across a voltage period, allows to properly consider the longer time scale plasma events (electron peak, after-glow). Indeed, it is noteworthy that the model predicts 99.997% of formed $CH_4(\nu 2, 4)$ to convert back to ground state methane via VT processes, with only a minute fraction of the species further leading to CH_3 production (0.003%) within this time period. Clearly, in the simulated conditions, and different time scales considered, the model does not show the vibrational excitation to be a driving conversion channel of methane, in line with the modelling study of Heijkers et al. (2020) and the experimental work of Butterworth et al. (2020). Indeed, $CH_4(\nu 2, 4)$ is only responsible for 0.012% of CH_3 creation, with the ground state contribution being higher at 14.35%. $CH_4^*(7.9eV)$ remains the major source of CH_3 at a contribution of 77.57%, indicating that the latter's pronounced creation during the two short electron energy peak events and at the positive peak of the voltage amplitude (Figure 3(a)) is still dominant across the entire period. This is further underlined by the existence of a net production of ground state methane from CH_3 radicals (12.79% of the latter's total consumption) due to the below recombination reaction:

$$CH_3 + H + M \rightarrow CH_4 + M$$

Importantly, the vibrational excitation-deexcitation loop takes place at much higher rates than those of the reactive processes, in line with the discussion in Section 4.3, where the energy spent on vibrational excitation of methane was estimated to be 55.5% of the total energy consumption.

Ethane

A product of methane upgrading, ethane primarily originates from methyl radicals (Figure 12(c)), 64.20% of which couple towards the species according to:

$$CH_3 + CH_3 + M \rightarrow C_2H_6 + M$$

From the ground state, 66.01% of ethane excites to the higher vibrational level $C_2H_6(\nu 1, 3)$, which almost exclusively deexcites to the lower level via VV collisions (Figure 11(b)). As with methane, the lower vibrational level $C_2H_6(\nu 2, 4)$ is mainly returning back to ground state ethane due to VT collisions. A significant fraction of ground state ethane (33.64%) dehydrogenates to ethylene according to the electron collision:

$$e^- + C_2H_6 \rightarrow C_2H_4 + H_2 + e^-$$

Because of the large extend of $C_2H_6(\nu 2, 4)$ and $C_2H_6(\nu 1, 3)$ deexcitation, these species only contribute to 0.099%

and 0.11% of the total formation of ethylene from the ethane lump, via equivalent electron impact processes to that of the ground state, which, nonetheless, proceed at comparable rates to the ground state reaction due to the low internal energy of the $v2,4$ and $v1,3$ states:

$$e^- + C_2H_6(\nu 2,4) \rightarrow C_2H_4 + H_2 + e^-$$

$$e^- + C_2H_6(\nu 1,3) \rightarrow C_2H_4 + H_2 + e^-$$

The creation of acetylene from ethane only accounts for 0.34% of ethane conversion (Figure 11(b)), mainly taking place via the following reaction:

$$C_2H + C_2H_6 \rightarrow C_2H_2 + C_2H_5$$

As will be discussed below, this process makes minor contribution (0.57%) to the total creation of acetylene, which dominantly takes place via ethylene.

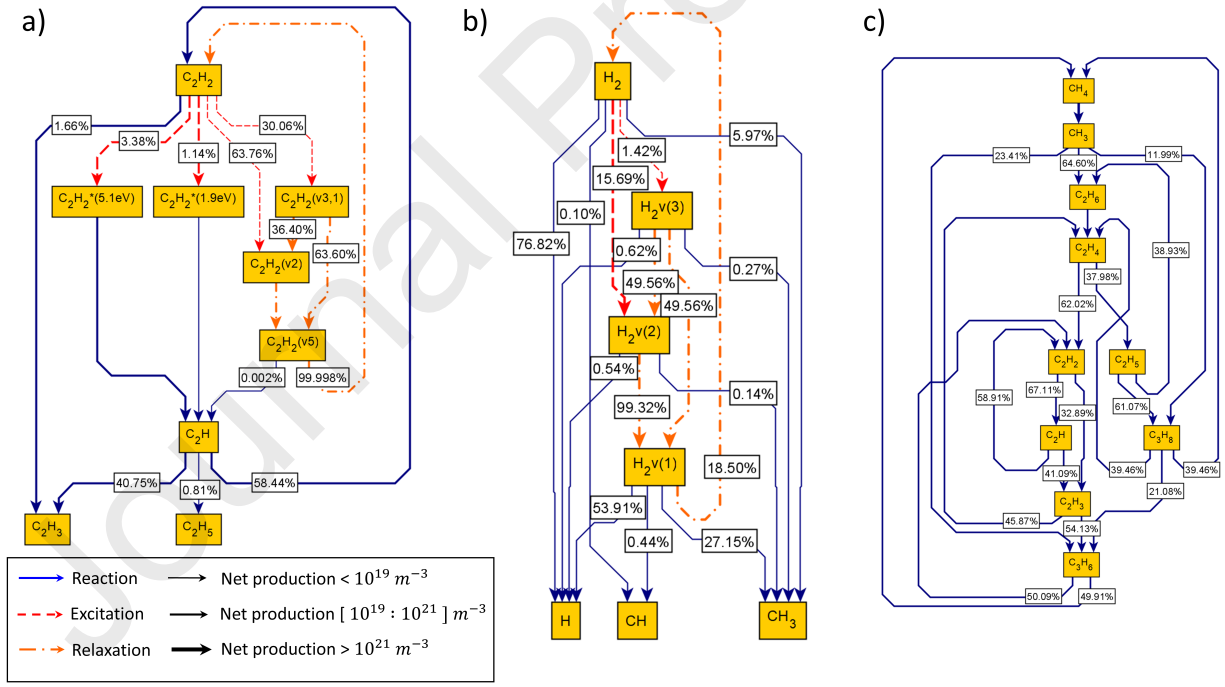

Figure 12: Integral reaction pathway analysis for (a) C_2H_2, (b) H_2, (c) the overall process (considering lumps for the molecules), across a voltage period for a reactor of 0.1 s residence time in quasi steady state.

Ethylene

As discussed above, ethylene production takes place mainly via the electron impact dissociation of ethane,

whereas its various excited states act as intermediates to its chemical conversion. In line with observations for other molecules, the creation of vibrationally excited states dominates the conversion of the ground state with 55.51% of ethylene getting excited to $C_2H_4(\nu 2)$. Electronical excitations $C_2H_4^*(5.0eV)$ and $C_2H_4^*(3.80eV)$ are less important at a 17.06% and 0.71% contribution to the conversion of ground state ethylene, respectively (Figure 11(c)).

Ethylene is the primary source of acetylene, according to the pathways below:

$$e^- + C_2H_4 \rightarrow C_2H_2 + H_2 + e^-$$

$$C_2H + C_2H_4 \rightarrow C_2H_2 + C_2H_3$$

where the electron collision involving C_2H_4 is responsible for 13.84% and the recombination with C_2H for 28.68% of the total production of acetylene. The processes involving low-energy excited states of ethylene:

$$e^- + C_2H_4(\nu 1) \rightarrow C_2H_2 + H_2 + e^-$$

$$e^- + C_2H_4^*(3.80eV) \rightarrow C_2H_2 + H_2 + e^-$$

$$C_2H + C_2H_4(\nu 1) \rightarrow C_2H_2 + C_2H_3$$

account only for 0.09%, 0.07%, 0.17% of acetylene's total production, with the rest being mainly due to C_3H_6 (Figure 12(c)), which accounts for 37.08%.

In addition, ethylene and its excited states contribute at varying degrees to the creation of C_2H_3 and C_2H_5 radicals as shown on Figures 11(c) and 12(c). C_2H_5 originates mainly from C_2H_4 (95.04% of its total creation), while the creation from $C_2H_4(\nu 1)$ and $C_2H_4^*(3.80eV)$ is negligible. For the case of C_2H_3, the higher energy electronically excited state $C_2H_4^*(5.0eV)$ is seen to exclusively pre-dissociate rapidly to C_2H_3 and H, accounting for 43.9% of the total formation of C_2H_3. The lower energy electronically excited state $C_2H_4^*(3.80eV)$, does not possess sufficiently high internal energy to pre-dissociate, however it still contributes via equivalent to the ground state electron collisions as discussed above. Interestingly, a net production of C_2H_4 from the hydrogenation of C_2H_3 is observed, as indicated by the recycle loops on both Figure 11(c) and 12(c).

Acetylene

Acetylene is the terminal stable species of the scheme. It mostly dehydrogenates to C_2H via the following electron collision, which accounts for 16.08% of its total consumption:

$$e^- + C_2H_2 \rightarrow C_2H + H + e^-$$

A larger fraction (58.99%) of the conversion of acetylene takes place through its electronical excitation and the subsequent pre-dissociation reaction:

$$C_2H_2^*(5.1eV) \rightarrow C_2H + H$$

Once created, 58.44% (Figure 12(a)) of C_2H radicals hydrogenate back to C_2H_2, accounting for 44.14% of acetylene's total creation (the rest originating from ethylene's dehydrogenation). The hydrogenation happens via reactions with methane, ethylene, and the lower energy vibrational state of dihydrogen:

$$C_2H + CH_4 \rightarrow C_2H_2 + CH_3$$

$$C_2H_4 + C_2H \rightarrow C_2H_2 + C_2H_3$$

$$C_2H + H_2\nu(1) \rightarrow C_2H_2 + H$$

These processes account for 13.85%, 28.68% and 1.18% of the total production of acetylene from C_2H radicals, respectively. The rest of the C_2H radicals re-hydrogenate into C_2H_3 (40.75%) and C_2H_5 (0.81%), which either gain one more hydrogen radical to become C_2H_4 and C_2H_6 or lead to the creation of C_3 compounds as shown on Figure 12(c).

Considering these pathways, acetylene is essentially found to undergo cycles of dehydrogenation to C_2H that further on mainly hydrogenates back to C_2H_2. The C_2H radicals are created during the peak when the electrons are energetic, while the hydrogenation happens immediately after the peak. Considering that acetylene is a terminal product, its periodic excitation and deexcitation and re-hydrogenation can be interpreted as an energy loss mechanism that impacts negatively the efficiency of the process.

Dihydrogen

Dihydrogen is predicted to be created mostly by electron collisions with ethane, which account for 74.03% of its creation, when the equivalent collisions with $C_2H_6(\nu 2, 4)$ and $C_2H_6(\nu 1, 3)$ amount only to 0.19% and 0.22%. The electron collisions with propane and methane are also found to be significant, accounting for 12.24% and 11.48%, respectively:

$$e^- + C_2H_6 \rightarrow C_2H_4 + H_2 + e^-$$

$$e^- + C_2H_6(\nu 2, 4) \rightarrow C_2H_4 + H_2 + e^-$$

$$e^- + C_2H_6(\nu 1, 3) \rightarrow C_2H_4 + H_2 + e^-$$

$$e^- + C_3H_8 \rightarrow C_3H_6 + H_2 + e^-$$

$$e^- + CH_4 \rightarrow CH_2 + H_2 + e^-$$

Once formed, 17.11% of dihydrogen excites into its vibrational states at contributions that are inversely related

to the energy threshold of the respective states (see Figure 12(b)). $H_2\nu(3)$ and $H_2\nu(2)$ contain sufficient internal energy to promote the radical producing reactions:

$$H_2\nu(3,2) + CH_2 \rightarrow CH_3 + H$$

$$e^- + H_2\nu(3,2) \rightarrow H + H + e^-$$

Nonetheless, the $v(2)$ and $v(3)$ levels of dihydrogen are also strongly subjected to the fast VV relaxation processes:

$$H_2 + H_2\nu(3) \rightarrow H_2\nu(2) + H_2\nu(1)$$

$$H_2 + H_2\nu(2) \rightarrow H_2\nu(1) + H_2\nu(1)$$

that are responsible for 99.32% and 99.12% of their respective consumption. Similarly to other species, the VT relaxation of the lowest level makes $H_2\nu(1)$ recycle back to the ground state (Figure 12(b)).

4.5 Effect of the residence time on the consumption of each species lump

The effect of the reactor residence time on the contribution of the different excitation modes to the conversion of their lumps is further discussed based on the results summarized in Table 3. In this table, the percentage of chemical conversion that proceeds through an excited state, or only the ground state, is presented for various species. These integral contribution results are obtained over an entire time-period of the applied voltage for reactors of different residence times that have reached a quasi steady state, with the contribution of mode j to the consumption of the whole lump calculated as follows:

$$Contribution(j) = \frac{\sum_{i=1}^{n_{channels}} Q(j)_i}{\sum_{k=1}^{n_{modes}} \left(\sum_{i=1}^{n_{channels}} Q(k)_i \right)} \tag{31}$$

Clear variations are observed for all species, linked with the composition of the gas at the equivalent conversion obtained for each residence time once quasi steady state is achieved. The role of excited states in the conversion of methane can be measured by considering their contribution to the conversion of the methane lump. For an entire applied voltage period, $CH_4(\nu 2,4)$, $CH_4(\nu 1,3)$ and $CH_4^*(7.9eV)$ are found to account for 0.153%, 0.006% and 79.17% of the total conversion of methane, respectively, at a reactor residence time of 0.1s (see Table 3) with the ground state being responsible for 20.67%. The above results clearly evidence that it is the electronic excitation channel that drives the conversion of methane. The relative importance of these channels varies with the residence time of the reactor. The rising residence time, indeed, leads to a reduction of the contribution of $CH_4^*(7.9eV)$ and a

respective increase of that of CH_4 due the latter's enhanced reaction with C_2H radicals that become more populous with the higher density of C_2H_2, as the conversion increases.

For the case of dihydrogen, the importance of $H_2\nu(1)$ decreases with the increasing density of H_2, the latter being an effective collisional partner for VT processes. The higher energy vibrational levels only have a minor impact on the species's total conversion due to the VV relaxation processes. The overall higher contribution of the excited states to dihydrogen's conversion makes the species one of the most sensitive to the presence of vibrational states.

For ethane, both vibrational levels $C_2H_6(\nu 2, 4)$ and $C_2H_6(\nu 1, 3)$ do not enable new channels of transformation. Due to their low densities these states are only responsible for less than 1% of the total consumption of the ethane lump for the entire range of residence times studied (Table 3). The contribution of $C_2H_6(\nu 2, 4)$ shows a slight decrease when residence time increases from 0.01 to 0.1 s, due to the rising density of H_2 that dominates its relaxation by VT collisions. Ethylene and acetylene both exhibit similar behavior to methane with the pre-dissociation of the higher energy electronically excited state being the main conversion contributor at low residence times, and its importance decreasing at longer contact times as the very reactive C_2H radicals become more populous.

Propane is the only species whose higher vibrational level has a higher contribution to the lower level at all residence times. Unlike other species, the higher energy mode is not quenched sufficiently fast via VV processes towards the lower energy one, due to the difference in their internal energies not being substantial enough. Propylene's excited mode shows a minor impact to the conversion of the lump due to its VT collisions with ground state methane that are quenching it very effectively at rates comparable to its formation via electron collisions with the ground state.

Table 3: Contribution of excited modes towards the total chemical conversion of each molecule's lump. Integral values presented across a time-period of the applied voltage, at reactors in quasi steady state, for different residence times.

Species	State	Conversion from the state (%)		
		$\tau = 0.01s$	$\tau = 0.1s$	$\tau = 0.5s$
CH_4	$Ground$	15.41	20.67	39.98
	$\nu 2, 4$	0.104	0.153	0.300
	$\nu 1, 3$	0.009	0.006	0.005
	$7.9eV$	84.48	79.17	59.72
H_2	$Ground$	74.78	93.34	93.06
	$\nu(1)$	23.75	6.511	6.460
	$\nu(2)$	1.297	0.138	0.435
	$\nu(3)$	0.176	0.007	0.044
C_2H_6	$Ground$	99.21	99.46	99.56
	$\nu 2, 4$	0.365	0.251	0.109
	$\nu 1, 3$	0.418	0.287	0.326
C_2H_4	Gd	51.42	63.90	82.86
	$\nu 1$	0.632	0.231	0.912
	$\nu 2$	0.020	0.015	0.008
	$3.8eV$	0.106	0.073	0.056
	$5.0eV$	47.81	35.78	16.08
C_2H_2	$Ground$	39.25	40.89	39.76
	$\nu 5$	0.210	0.036	0.043
	$\nu 2$	0.224	0.018	0.022
	$\nu 3, 1$	0.013	0.004	0.002
	$1.9eV$	0.069	0.057	0.057
	$5.1eV$	60.23	58.99	60.11
C_3H_8	$Ground$	88.19	92.03	92.30
	$\nu 1$	1.549	1.105	1.602
	$\nu 2$	10.26	6.860	6.089
C_3H_6	$Ground$	99.46	99.51	99.48
	$\nu 1$	0.540	0.490	0.518

5 Conclusions

A detailed kinetic network of low temperature methane plasma is developed. The scheme includes the reactivity and the relaxation processes of electronically and vibrationally excited species along with negative ions. Modelling is performed using this scheme of the methane upgrading process in a dielectric barrier discharge flow reactor, using a combined zero-dimensional and one-dimensional modelling approach.

Qualitative agreement is found between the modelling and the experimental results for the selectivities, whereas quantitative agreement is achieved for the conversions. The role of excited molecules is found to be significant in the methane upgrading process. Indeed, the majority of the provided energy is consumed by the creation of excited states. Many low energy vibrationally excited states are created during short electron streamers, however due to rapid VV and VT processes, these species are mostly quenched soon after their creation, in compliance with

experimental literature. Consequently, only a reduced fraction of the conversion of molecules takes place via some of their vibrationally excited modes (0.16% for methane, 6.66% for H_2, 0.54% for C_2H_6 at a reactor residence time of 0.1s). The higher energy vibrationally excited species are much less populous than the lower energy states as they generally deexcite due to very fast VV relaxation processes. Electronically excited species with high internal energy are found to be very effective at promoting conversion. Around 79.17% of methane conversion proceeds through the electronically excited state $CH_4^*(7.9eV)$ for a 0.1 s reactor residence time. Over long-time scales the reactor carbon balance is found to be highly sensitive to the sticking coefficients of radicals, underlining the need to take into account the effect of the saturation of species densities onto the walls, and surface chemical reactions, for more accurate future modelling. Further enhancements to the kinetic scheme could relate to including reactions between vibrational modes of different species, accounting for the excitation of vibrationally excited states into higher vibrational levels, and considering excited modes of the radicals and their reactivity.

Most importantly, the present modelling results highlight the importance of developing processes that efficiently utilize the internal energy of vibrationally excited states to enhance chemical transformations. Indeed, the selective transformation of these states on the surface of a catalyst before their quenching in the gas phase could drastically enhance energy efficiency. Having explicitly considered the reactivity of the excited states in the plasma phase, it is possible to interface the current model with heterogeneous catalytic micro-kinetic models to allow the elucidation of the complex reaction dynamics of plasma-catalysis systems.

Nomenclature

Symbols

a	Parameter set to 1 if the drift velocity is directed to the wall, 0 otherwise (-)
$\frac{A}{V}$	Surface area/volume ratio of the annular reactor (m^{-1})
$C_{balance}$	Carbon balance (%)
$c_{p,r}$	Net stoichiometric coefficient of species p in reaction r (-)
D	Diffusion coefficient ($m^2.s^{-1}$)
$\overrightarrow{E}$	Electric field vector ($V.m^{-1}$)
$\frac{E}{N}$	Reduced electric field ($V.m^2$)
E_a	Activation energy ($J.mol^{-1}$)
E_ν	Vibrational energy ($J.mol^{-1}$)
$\overrightarrow{\mathrm{j}}$	Density of the transport flux vector ($m^{-3}.s^{-1}$)

$k_{m-1\rightarrow m}^{n\rightarrow n-1}$	Rate constant for a VV process where a species excites from mode/level $m-1$ to m via the deexcitation of the another species from mode/level n to $n-1$ ($m^3.s^{-1}$)
k_B	Boltzmann's constant ($1.38064852.10^{-23} m^2.kg.s^{-2}.K^{-1}$)
k_R	Rate constant ($m^3.s^{-1}$)
k_{R0}	Pre-exponential factor ($m^3.s^{-1}$)
k_{VT}^{10}	Rate constant of VT process where a single-quantum excited species returns to ground state ($m^3.s^{-1}$)
L_{elast}	Electron energy density lost due to elastic collisions ($J.m^{-3}$)
$L_{reflection}$	Rate of ground state species reflecting from the wall back into the vessel ($m^{-3}.s^{-1}$)
M	Mass of a species (kg)
m_{ij}	Reduced mass of colliding species i and j (atomic unit)
$\overrightarrow{n}$	Unit vector (-)
n	Number density (m^{-3})
$P_{m-1\rightarrow m}^{n\rightarrow n-1}$	Probability for a VV process where a species excites from mode/level $m-1$ to m via the deexcitation of the other species from mode/level n to $n-1$ to happen (-)
p	Pressure (Pa)
P_d	Power density deposition ($J.m^{-3}$)
q	Elementary charge ($1.60217662.10^{-19} C$)
Q	Integral of rate (m^{-3})
r_A	Radius of particle A (m)
R_d	Internal radius of dielectric (m)
R_e	Outer radius of dielectric (m)
R_g	Radius of ground electrode (m)
r_r	Reaction rate ($m^{-3}.s^{-1}$)
S	Source term ($m^{-3}.s^{-1}$)

s	Sticking coefficient (-)
$S_{C_xH_y}$	Selectivity of species C_xH_y (%)
t	Time (s)
T_0	Temperature of the bulk gas (K)
T_e	Electron temperature (K)
$U_{th,r}$	Energy threshold of electron collision r (J)
V_0	Voltage amplitude (V)
X_{CH_4}	Methane conversion (%)

687 Greek letters

α	Coefficient of efficiency of the excitation energy in overcoming the activation energy (-)
α_i	Polarizability of the background gas (m^3)
ε	Local average electron energy (J)
ε_0	Permittivity of free space ($\approx 8.85.10^{-12} F.m^{-1}$)
ε_{ij}	Characteristic energy in the 12-6 Lennard-Jones potential (J)
ε_r	Relative permittivity of the dielectric (-)
θ	Heaviside function (-)
Θ	Characteristic temperature of the excited species (K)
$\mu_{i,j}$	Ion mobility coefficient ($m^2.V^{-1}.s^{-1}$)
v_{th}	Thermal velocity ($m.s^{-1}$)
ρ	Surface charge density ($C.m^{-2}$)
$\sigma_{i,j}$	Characteristic length in the 12-6 Lennard-Jones potential (J)
τ	Residence time of the reactor (s)
γ	Secondary electron emission coefficient (-)

φ	Electric potential (φ)
Ψ	Dimensionless temperature (-)
ω	Angular frequency of the applied voltage ($rad.s^{-1}$)
Ω_D	Collision integral (-)

Subscripts

0	Ground state of a species
$diel$	Dielectric
$feed$	Feed flow into the reactor
$lump$	Sum of all the states of a molecule
p	Refers to any species
α	Refers to ions (α^+ for the case of positive ions, α^- for the case of negative ones)
β	Refers to neutral species
$\beta*$	Refers to the electronically excited states of species β
β_0	Refers to inlet flow of species β
ε	Refers to the local average electron energy
ν	Refers to energy, number density of vibrationally excited species

Acknowledgments

We acknowledge and greatly appreciate the assistance from Dr. Mihailova from Plasma Matters B.V. in working with the software Plasimo and from Dr Marcus Campbell Bannerman from the University of Aberdeen for providing access to the computational cluster used for carrying out the simulations in this work.

The work was supported by the UK Engineering and Physical Sciences Research Council (EPSRC) New Investigator Award, grant no. EP/R031800/1.

References

Agiral, A., Trionfetti, C., Lefferts, L., Seshan, K., Gardeniers, J.G.E., 2008. Propane Conversion at Ambient Temperatures C-C and C-H Bond Activation Using Cold Plasma in a Microreactor. Chem. Eng. Technol. 31. URL: https://onlinelibrary.wiley.com/doi/abs/10.1002/ceat.200800175, doi:10.1002/ceat.200800175.

Bai, C., Wang, L., Li, L., Dong, X., Xiao, Q., Liu, Z., Sun, J., Pan, J., 2019. Numerical investigation on the CH_4/CO_2 nanosecond pulsed dielectric barrier discharge plasma at atmospheric pressure. AIP Adv. 9, 035023. URL: https://aip.scitation.org/doi/10.1063/1.5063519, doi:10.1063/1.5063519.

Bera, K., Farouk, B., Lee, Y.H., 1999. Effects of reactor pressure on two-dimensional radio-frequency methane plasma: a numerical study. Plasma Sources Sci. Technol. 8, 412–420. URL: https://doi.org/10.1088%2F0963-0252%2F8%2F3%2F311, doi:10.1088/0963-0252/8/3/311.

Bera, K., Farouk, B., Vitello, P., 2001. Inductively coupled radio frequency methane plasma simulation. J. Phys. D Appl. Phys. 34, 1479–1490. URL: https://doi.org/10.1088%2F0022-3727%2F34%2F10%2F308, doi:10.1088/0022-3727/34/10/308.

Bleecker, K.D., Herrebout, D., Bogaerts, A., Gijbels, R., Descamps, P., 2003. One-dimensional modelling of a capacitively coupled rf plasma in silane/helium, including small concentrations of O_2 and N_2. J. Phys. D Appl. Phys. 36, 1826–1833. URL: https://doi.org/10.1088%2F0022-3727%2F36%2F15%2F313, doi:10.1088/0022-3727/36/15/313.

Bogaerts, A., Kozák, T., van Laer, K., Snoeckx, R., 2015. Plasma-based conversion of CO_2 : current status and future challenges. Faraday Discuss. 183, 217–232. URL: http://xlink.rsc.org/?DOI=C5FD00053J, doi:10.1039/C5FD00053J.

Bogaerts, A., Zhang, Q.Z., Zhang, Y.R., Van Laer, K., Wang, W., 2019. Burning questions of plasma catalysis: Answers by modeling. Catal. Today 337, 3–14. URL: http://www.sciencedirect.com/science/article/pii/S0920586119302111, doi:10.1016/j.cattod.2019.04.077.

Böttcher, C.J.F., 1973. Theory of Electric Polarization. Elsevier scientific publishing company. URL: https://www.sciencedirect.com/book/9780444410191/theory-of-electric-polarization#book-description.

Braun, D., Gibalov, V., Pietsch, G., 1992. Two-dimensional modelling of the dielectric barrier discharge in air. Plasma Sources Sci. Technol. 1, 166. URL: http://stacks.iop.org/0963-0252/1/i=3/a=004, doi:10.1088/0963-0252/1/3/004.

Butterworth, T., Steeg, A.v.d., Bekerom, D.v.d., Minea, T., Righart, T., Ong, Q., Rooij, G.v., 2020. Plasma induced vibrational excitation of CH_4—a window to its mode selective processing. Plasma Sources Sci. Technol. 29, 095007. URL: https://iopscience.iop.org/article/10.1088/1361-6595/aba1c9/meta, doi:10.1088/1361-6595/aba1c9. publisher: IOP Publishing.

De Bie, C., van Dijk, J., Bogaerts, A., 2015. The Dominant Pathways for the Conversion of Methane into Oxygenates and Syngas in an Atmospheric Pressure Dielectric Barrier Discharge. J. Phys. Chem. C 119, 22331–22350. URL: http://pubs.acs.org/doi/10.1021/acs.jpcc.5b06515, doi:10.1021/acs.jpcc.5b06515.

De Bie, C., Verheyde, B., Martens, T., van Dijk, J., Paulussen, S., Bogaerts, A., 2011. Fluid Modeling of the Conversion of Methane into Higher Hydrocarbons in an Atmospheric Pressure Dielectric Barrier Discharge. Plasma Process. Polym. 8, 1033–1058. URL: https://onlinelibrary.wiley.com/doi/abs/10.1002/ppap.201100027, doi:10.1002/ppap.201100027.

De Vasconcelos, M.H., 1976. Vibrational relaxation times in methane: The optic-acoustic effect. Ph.D. thesis. University of Amsterdam.

Delikonstantis, E., Scapinello, M., Van Geenhoven, O., Stefanidis, G.D., 2020. Nanosecond pulsed discharge-driven non-oxidative methane coupling in a plate-to-plate electrode configuration plasma reactor. Chem. Eng. J. 380, 122477. URL: http://www.sciencedirect.com/science/article/pii/S1385894719318807, doi:10.1016/j.cej.2019.122477.

Dijk, J.v., Peerenboom, K., Jimenez, M., Mihailova, D., Mullen, J.v.d., 2009. The plasma modelling toolkit Plasimo. J. Phys. D: Appl. Phys. 42, 194012. URL: http://stacks.iop.org/0022-3727/42/i=19/a=194012, doi:10.1088/0022-3727/42/19/194012.

van Dishoeck, E.F., Black, J.H., 1988. The photodissociation and chemistry of interstellar CO. Astrophys. J. 334, 771. URL: http://adsabs.harvard.edu/doi/10.1086/166877, doi:10.1086/166877.

Dors, M., Nowakowska, H., Jasiński, M., Mizeraczyk, J., 2014. Chemical Kinetics of Methane Pyrolysis in Microwave Plasma at Atmospheric Pressure. Plasma Chem. Plasma P. 34, 313–326. URL: http://link.springer.com/10.1007/s11090-013-9510-4, doi:10.1007/s11090-013-9510-4.

Eckert, M., Neyts, E., Bogaerts, A., 2008. Molecular Dynamics Simulations of the Sticking and Etch Behavior of Various Growth Species of (Ultra)Nanocrystalline Diamond Films. Chem. Vap. Depos. 14, 213–223. URL: https://onlinelibrary.wiley.com/doi/abs/10.1002/cvde.200706657, doi:10.1002/cvde.200706657.

Efremov, A.M., Semenova, O.A., Barinov, S.M., 2015. Influence of the initial composition of a methane-argon mixture on the electricophysical parameters and plasma composition of DC glow discharge. High Temp. 53, 171–178. URL: https://doi.org/10.1134/S0018151X1406008X, doi:10.1134/S0018151X1406008X.

Engelmann, Y., Mehta, P., Neyts, E.C., Schneider, W.F., Bogaerts, A., 2020. Predicted Influence of Plasma Activation on Nonoxidative Coupling of Methane on Transition Metal Catalysts. ACS Sustainable Chem. Eng. 8, 6043–6054. URL: https://doi.org/10.1021/acssuschemeng.0c00906, doi:10.1021/acssuschemeng.0c00906. publisher: American Chemical Society.

Fan, W.Y., Knewstubb, P.F., Käning, M., Mechold, L., Röpcke, J., Davies, P.B., 1999. A Diode Laser and Modeling Study of Mixed (CH_4-H_2-O_2) AC Plasmas. J. Phys. Chem. A 103, 4118–4128. URL: https://doi.org/10.1021/jp9845701, doi:10.1021/jp9845701.

Farouk, T., Farouk, B., Gutsol, A., Fridman, A., 2008. Atmospheric pressure methane-hydrogen dc micro-glow discharge for thin film deposition. J. Phys. D Appl. Phys. 41. URL: https://iopscience.iop.org/article/10.1088/0022-3727/41/17/175202/meta, doi:10.1088/0022-3727/41/17/175202.

Ferrara, C., Preda, M., Cavallotti, C., 2012. On the streamer propagation in methane plasma discharges. J. Appl. Phys. 112, 113301. URL: https://doi.org/10.1063/1.4766299, doi:10.1063/1.4766299.

Fincke, J.R., Anderson, R.P., Hyde, T., Detering, B.A., Wright, R., Bewley, R.L., Haggard, D.C., Swank, W.D., 2002. Plasma Thermal Conversion of Methane to Acetylene. Plasma Chem. Plasma P. 22, 105–136. URL: https://doi.org/10.1023/A:1012944615974, doi:10.1023/A:1012944615974.

Fridman, A., 2008. Plasma Chemistry. Cambridge University Press. doi:10.1017/CBO9780511546075.

Gao, C.W., Allen, J.W., Green, W.H., West, R.H., 2016. Reaction Mechanism Generator: Automatic construction of chemical kinetic mechanisms. Comput. Phys. Commun. 203, 212 – 225. URL: http://www.sciencedirect.com/science/article/pii/S0010465516300285, doi:10.1016/j.cpc.2016.02.013.

Gao, Y., Zhang, S., Sun, H., Wang, R., Tu, X., Shao, T., 2018. Highly efficient conversion of methane using microsecond and nanosecond pulsed spark discharges. Appl. Energy 226, 534–545. URL: https://linkinghub.elsevier.com/retrieve/pii/S0306261918308730, doi:10.1016/j.apenergy.2018.06.006.

Gilbert, D.P., Roeder, D.M., Thornley, D.P., 2013. Can the UK afford (not) to produce chemicals in 2050? Technical Report. Tyndall Manchester.

Gogolides, E., Buteau, C., Rhallabi, A., Turban, G., 1994. Radio-frequency glow discharges in methane gas: modelling of the gas-phase physics and chemistry. J. Phys. D Appl. Phys. 27, 818–825. URL: https://doi.org/10.1088%2F0022-3727%2F27%2F4%2F020, doi:10.1088/0022-3727/27/4/020.

Hagelaar, G.J.M., Pitchford, L.C., 2005. Solving the Boltzmann equation to obtain electron transport coefficients and rate coefficients for fluid models. Plasma Sources Sci. Technol. 14, 722–733. URL: http://stacks.iop.org/0963-0252/14/i=4/a=011, doi:10.1088/0963-0252/14/4/011.

Heijkers, S., Aghaei, M., Bogaerts, A., 2020. Plasma-Based CH_4 Conversion into Higher Hydrocarbons and H_2 : Modeling to Reveal the Reaction Mechanisms of Different Plasma Sources. J. Phys. Chem. C 124, 7016–7030. URL: https://pubs.acs.org/doi/10.1021/acs.jpcc.0c00082, doi:10.1021/acs.jpcc.0c00082.

Herrebout, D., Bogaerts, A., Yan, M., Gijbels, R., Goedheer, W., Dekempeneer, E., 2001. One-dimensional fluid model for an rf methane plasma of interest in deposition of diamond-like carbon layers. J. Appl. Phys. 90, 570–579. URL: https://doi.org/10.1063/1.1378059, doi:10.1063/1.1378059.

Herrebout, D., Bogaerts, A., Yan, M., Gijbels, R., Goedheer, W., Vanhulsel, A., 2002. Modeling of a capacitively coupled radio-frequency methane plasma: Comparison between a one-dimensional and a two-dimensional fluid model. J. Appl. Phys. 92, 2290–2295. URL: https://doi.org/10.1063/1.1500789, doi:10.1063/1.1500789.

Hill, G.L., Winter, T.G., 1968. Effect of Temperature on the Rotational and Vibrational Relaxation Times of Some Hydrocarbons. J. Chem. Phys. 49, 440–444. URL: http://aip.scitation.org/doi/10.1063/1.1669842, doi:10.1063/1.1669842.

Hurlbatt, A., Gibson, A.R., Schröter, S., Bredin, J., Foote, A.P.S., Grondein, P., O'Connell, D., Gans, T., 2017. Concepts, Capabilities, and Limitations of Global Models: A Review. Plasma Process. Polym. URL: https://onlinelibrary.wiley.com/doi/abs/10.1002/ppap.201600138, doi:10.1002/ppap.201600138.

Indarto, A., Choi, J.W., Lee, H., Keun Song, H., 2005. Kinetic modeling of plasma methane conversion using gliding arc. J. Nat. Gas Chem. 14, 13–21.

Indarto, A., Coowanitwong, N., Choi, J.W., Lee, H., Song, H.K., 2008. Kinetic modeling of plasma methane conversion in a dielectric barrier discharge. Fuel Process. Technol. 89, 214 – 219. URL: http://www.sciencedirect.com/science/article/pii/S0378382007001956, doi:10.1016/j.fuproc.2007.09.006.

Juurlink, L.B.F., Killelea, D.R., Utz, A.L., 2009. State-resolved probes of methane dissociation dynamics. Prog. Surf. Sci. 84, 69–134. URL: http://adsabs.harvard.edu/abs/2009PrSS...84...69J, doi:10.1016/j.progsurf.2009.01.001.

Kechagiopoulos, P.N., Thybaut, J.W., Marin, G.B., 2014. Oxidative coupling of methane: A microkinetic model accounting for intraparticle surface-intermediates concentration profiles. Ind. Eng. Chem. Res. 53, 1825–1840. URL: https://doi.org/10.1021/ie403160s, doi:10.1021/ie403160s.

Khadir, N., Khodja, K., Be, A., 2017. Methane conversion using a dielectric barrier discharge reactor at atmospheric pressure for hydrogen production. Plasma Sci. Technol. 19, 095502. URL: https://doi.org/10.1088%2F2058-6272%2Faa6d6d, doi:10.1088/2058-6272/aa6d6d.

Khoja, A.H., Tahir, M., Amin, N.A.S., 2018. Cold plasma dielectric barrier discharge reactor for dry reforming of methane over Ni/γ-Al_2O_3-MgO nanocomposite. Fuel Process. Technol. 178, 166–179. URL: https://linkinghub.elsevier.com/retrieve/pii/S0378382018304739, doi:10.1016/j.fuproc.2018.05.030.

Khoja, A.H., Tahir, M., Amin, N.A.S., 2019a. Recent developments in non-thermal catalytic DBD plasma reactor for dry reforming of methane. Energy Convers. Manag. 183, 529 – 560. URL: http://www.sciencedirect.com/science/article/pii/S0196890419300330, doi:10.1016/j.enconman.2018.12.112.

Khoja, A.H., Tahir, M., Saidina Amin, N.A., 2019b. Process optimization of DBD plasma dry reforming of methane over Ni/$La_2O_3MgAl_2O_4$ using multiple response surface methodology. Int. J. Hydrog. 44, 11774–11787. URL: https://linkinghub.elsevier.com/retrieve/pii/S0360319919310158, doi:10.1016/j.ijhydene.2019.03.059.

Koelman, P., Heijkers, S., Tadayon Mousavi, S., Graef, W., Mihailova, D., Kozak, T., Bogaerts, A., van Dijk, J., 2017. A Comprehensive Chemical Model for the Splitting of CO_2 in Non-Equilibrium Plasmas: A Comprehensive Chemical Model for CO_2 Splitting. Plasma Process. Polym. 14, 1600155. URL: http://doi.wiley.com/10.1002/ppap.201600155, doi:10.1002/ppap.201600155.

Kozák, T., Bogaerts, A., 2014. Splitting of CO_2 by vibrational excitation in non-equilibrium plasmas: a reaction kinetics model. Plasma Sources Sci. Technol. 23, 045004. URL: http://stacks.iop.org/0963-0252/23/i=4/a=045004?key=crossref.ae2245ca0b3f38b3e8652fc96aea2549, doi:10.1088/0963-0252/23/4/045004.

Kraus, M., Egli, W., Haffner, K., Eliasson, B., Kogelschatz, U., Wokaun, A., 2002. Investigation of mechanistic aspects of the catalytic CO_2 reforming of methane in a dielectric-barrier discharge using optical emission spectroscopy and kinetic modeling. Phys. Chem. Chem. Phys. 4, 668–675. URL: http://dx.doi.org/10.1039/B108040G, doi:10.1039/B108040G.

Kudryashov, S.V., Ryabov, A.Y., Ochered'ko, A.N., 2018. Simulation of the Kinetics of Methane Conversion in the Presence of Water in a Barrier Discharge. High Energy Chem. 52, 167–170. URL: https://doi.org/10.1134/S0018143918020108, doi:10.1134/S0018143918020108.

Li, X.S., Zhu, A.M., Wang, K.J., Xu, Y., Song, Z.M., 2004. Methane conversion to C_2 hydrocarbons and hydrogen in atmospheric non-thermal plasmas generated by different electric discharge techniques. Catal. Today 98, 617–624. URL: http://linkinghub.elsevier.com/retrieve/pii/S0920586104006145, doi:10.1016/j.cattod.2004.09.048.

Lifshitz, A., 1974. Correlation of vibrational de-excitation rate constants (k0←1) of diatomic molecules. J. Chem. Phys. 61, 2478–2479. URL: https://doi.org/10.1063/1.1682359, doi:10.1063/1.1682359.

Liu, C.j., Mallinson, R., Lobban, L., 1998. Nonoxidative Methane Conversion to Acetylene over Zeolite in a Low Temperature Plasma. J. Catal. 179, 326 – 334. URL: http://www.sciencedirect.com/science/article/pii/S0021951798922254, doi:10.1006/jcat.1998.2225.

Luche, J., Aubry, O., Khacef, A., Cormier, J.M., 2009. Syngas production from methane oxidation using a non-thermal plasma: Experiments and kinetic modeling. Chem. Eng. J. 149, 35 – 41. URL: http://www.sciencedirect.com/science/article/pii/S1385894708006384, doi:10.1016/j.cej.2008.09.045.

Lunsford, J.H., 2000. Catalytic conversion of methane to more useful chemicals and fuels: a challenge for the 21st century. Catal. Today 63, 165 – 174. URL: http://www.sciencedirect.com/science/article/pii/S0920586100004569, doi:10.1016/S0920-5861(00)00456-9.

Maitre, P.A., Bieniek, M.S., Kechagiopoulos, P.N., 2020. Plasma-enhanced catalysis for the upgrading of methane: a review of modelling and simulation methods. React. Chem. Eng. 5, 814–837. URL: http://dx.doi.org/10.1039/D0RE00024H, doi:10.1039/D0RE00024H.

Masi, M., Cavallotti, C., Carrà, S., 1998. Different approaches for methane plasmas modeling. Chem. Eng. Sci. 53, 3875 – 3886. URL: http://www.sciencedirect.com/science/article/pii/S0009250998001973, doi:10.1016/S0009-2509(98)00197-3.

Menard-Bourcin, F., Boursier, C., Doyennette, L., Menard, J., 2005. Rotational and Vibrational Relaxation of Methane Excited to $2\nu_3$ in CH_4/H_2 and CH_4/He Mixtures at 296 and 193 K from Double-Resonance Measurements. J. Phys. Chem. A 109, 3111–3119. URL: https://pubs.acs.org/doi/10.1021/jp0448649, doi:10.1021/jp0448649.

Michielsen, I., Uytdenhouwen, Y., Bogaerts, A., Meynen, V., 2019. Altering Conversion and Product Selectivity of Dry Reforming of Methane in a Dielectric Barrier Discharge by Changing the Dielectric Packing Material. Catalysts 9, 51. URL: https://www.mdpi.com/2073-4344/9/1/51, doi:10.3390/catal9010051.

Molteni, M., Donazzi, A., 2020. Model analysis of atmospheric non-thermal plasma for methane abatement in a gas phase dielectric barrier discharge reactor. Chem. Eng. Sci. 212, 115340. URL: http://www.sciencedirect.com/science/article/pii/S0009250919308309, doi:https://doi.org/10.1016/j.ces.2019.115340.

Moss, M.S., Yanallah, K., Allen, R.W.K., Pontiga, F., 2017. An investigation of CO_2 splitting using nanosecond pulsed corona discharge: effect of argon addition on CO_2 conversion and energy efficiency. Plasma Sources Sci. Technol. 26, 035009. URL: https://doi.org/10.1088%2F1361-6595%2Faa5b1d, doi:10.1088/1361-6595/aa5b1d.

Naidis, G.V., 2007. Modelling of transient plasma discharges in atmospheric-pressure methane–air mixtures. J. Phys. D Appl. Phys. 40, 4525–4531. URL: https://doi.org/10.1088%2F0022-3727%2F40%2F15%2F024, doi:10.1088/0022-3727/40/15/024.

Naidis, G.V., 2018. Effects of photoionization characteristics on parameters of positive streamers. Plasma Res. Express 1, 017001. URL: https://doi.org/10.1088%2F2516-1067%2Faae73d, doi:10.1088/2516-1067/aae73d.

Neyts, E.C., 2016. Plasma-Surface Interactions in Plasma Catalysis. Plasma Chem. Plasma P. 36, 185–212. URL: http://link.springer.com/10.1007/s11090-015-9662-5, doi:10.1007/s11090-015-9662-5.

Nikitin, A.V., Protasevich, A.E., Rey, M., Tyuterev, V.G., 2018. Highly excited vibrational levels of methane up to 10 300 cm-1: Comparative study of variational methods. J. Chem. Phys. 149, 124305. URL: https://aip.scitation.org/doi/full/10.1063/1.5042154, doi:10.1063/1.5042154.

Nozaki, T., Muto, N., Kado, S., Okazaki, K., 2004. Dissociation of vibrationally excited methane on Ni catalyst. Catal. Today 89, 57–65. URL: http://linkinghub.elsevier.com/retrieve/pii/S0920586103006059, doi:10.1016/j.cattod.2003.11.040.

Nozaki, T., Okazaki, K., 2013. Non-thermal plasma catalysis of methane: Principles, energy efficiency, and applications. Catal. Today 211, 29–38. URL: http://linkinghub.elsevier.com/retrieve/pii/S092058611300148X, doi:10.1016/j.cattod.2013.04.002.

Pancheshnyi, S., Eismann, B., Hagelaar, G.J.M., Pitchford, L.C., 2008. Computer code ZDPlasKin. URL: http://www.zdplaskin.laplace.univ-tlse.fr. published: University of Toulouse, LAPLACE, CNRS-UPS-INP, Toulouse, France.

Pintassilgo, C.D., Jaoul, C., Loureiro, J., Belmonte, T., Czerwiec, T., 2007. Kinetic modelling of a N_2 flowing microwave discharge with CH_4 addition in the post-discharge for nitrocarburizing treatments. J. Phys. D Appl. Phys. 40, 3620–3632. URL: https://doi.org/10.1088%2F0022-3727%2F40%2F12%2F011, doi:10.1088/0022-3727/40/12/011.

Pitchford, L.C., Boeuf, J.P., Morgan, W.L., 1998. Boltzmann Simulation Software and Database.

Pourali, N., Foroutan, G., 2015. The effects of plasma inhomogeneity on the nanoparticle coating in a low pressure plasma reactor. Phys. Plasmas 22, 103514. URL: https://doi.org/10.1063/1.4933361, doi:10.1063/1.4933361.

Puliyalil, H., Lašič Jurković, D., Dasireddy, V.D.B.C., Likozar, B., 2018. A review of plasma-assisted catalytic conversion of gaseous carbon dioxide and methane into value-added platform chemicals and fuels. RSC Adv. 8, 27481–27508. URL: http://xlink.rsc.org/?DOI=C8RA03146K, doi:10.1039/C8RA03146K.

Qian, M., Li, G., Kang, J., Liu, S., Ren, C., Zhang, J., Wang, D., 2018. Fluid modeling of radical species generation mechanism in dense methane-air mixture streamer discharge. Phys. Plasmas 25, 013519. URL: https://doi.org/10.1063/1.5016855, doi:10.1063/1.5016855.

Ray, D., Nepak, D., Janampelli, S., Goshal, P., Subrahmanyam, C., 2019. Dry Reforming of Methane in DBD Plasma over Ni-Based Catalysts: Influence of Process Conditions and Support on Performance and Durability. Energy Technol. 7, 1801008. URL: https://onlinelibrary.wiley.com/doi/abs/10.1002/ente.201801008, doi:10.1002/ente.201801008.

Rusanov, A., Fridman, A., Sholin, G., 1981. The physics of a chemically active plasma with nonequilibrium vibrational excitation of molecules. Soviet Physics Uspekhi 24. URL: https://doi.org/10.1070%2Fpu1981v024n06abeh004884, doi:10.1070/pu1981v024n06abeh004884.

Saleem, F., Kennedy, J., Dahiru, U.H., Zhang, K., Harvey, A., 2019. Methane conversion to H_2 and higher hydrocarbons using non-thermal plasma dielectric barrier discharge reactor. Chem. Eng. Process. 142, 107557. URL: http://www.sciencedirect.com/science/article/pii/S0255270118315538, doi:10.1016/j.cep.2019.107557.

Scapinello, M., Delikonstantis, E., Stefanidis, G.D., 2017. The panorama of plasma-assisted non-oxidative methane reforming. Chem. Eng. Process. 117, 120–140. URL: http://linkinghub.elsevier.com/retrieve/pii/S0255270116306870, doi:10.1016/j.cep.2017.03.024.

Scapinello, M., Delikonstantis, E., Stefanidis, G.D., 2019. A study on the reaction mechanism of non-oxidative methane coupling in a nanosecond pulsed discharge reactor using isotope analysis. Chem. Eng. J. 360, 64–74. URL: https://linkinghub.elsevier.com/retrieve/pii/S1385894718323921, doi:10.1016/j.cej.2018.11.161.

Sheng, Z., Watanabe, Y., Kim, H.H., Yao, S., Nozaki, T., 2020. Plasma-enabled mode-selective activation of CH_4 for dry reforming: First touch on the kinetic analysis. Chem. Eng. J. 399. doi:10.1016/j.cej.2020.125751.

Snoeckx, R., Bogaerts, A., 2017. Plasma technology – a novel solution for CO_2 conversion? Chem. Soc. Rev. 46, 5805–5863. URL: http://xlink.rsc.org/?DOI=C6CS00066E, doi:10.1039/C6CS00066E.

Snoeckx, R., Setareh, M., Aerts, R., Simon, P., Maghari, A., Bogaerts, A., 2013. Influence of N_2 concentration in a CH_4/N_2 dielectric barrier discharge used for CH_4 conversion into H_2. Int. J. Hydrogen Energ. 38, 16098–16120. URL: http://linkinghub.elsevier.com/retrieve/pii/S0360319913023847, doi:10.1016/j.ijhydene.2013.09.136.

Song, M.Y., Yoon, J.S., Cho, H., Itikawa, Y., Karwasz, G.P., Kokoouline, V., Nakamura, Y., Tennyson, J., 2015. Cross Sections for Electron Collisions with Methane. J. Phys. Chem. Ref. Data 44, 023101. URL: http://aip.scitation.org/doi/10.1063/1.4918630, doi:10.1063/1.4918630.

Starikovskiy, A., Aleksandrov, N., 2013. Plasma-assisted ignition and combustion. Prog. Energy Combust. Sci. 39, 61–110. URL: http://www.sciencedirect.com/science/article/pii/S0360128512000354, doi:10.1016/j.pecs.2012.05.003.

Sun, J., Chen, Q., 2019. Kinetic roles of vibrational excitation in RF plasma assisted methane pyrolysis. J. Energy Chem. 39, 188 – 197. URL: http://www.sciencedirect.com/science/article/pii/S2095495618312002, doi:10.1016/j.jechem.2019.01.028.

Tachibana, K., Nishida, M., Harima, H., Urano, Y., 1984. Diagnostics and modelling of a methane plasma used in the chemical vapour deposition of amorphous carbon films. J. Phys. D Appl. Phys. 17, 1727–1742. URL: https://doi.org/10.1088%2F0022-3727%2F17%2F8%2F026, doi:10.1088/0022-3727/17/8/026.

Toth, J.R., Shen, X., Lacks, D.J., Sankaran, R.M., 2018. Reaction Conversion for a Plasma-Based Steady-State Flow Process Is Independent of Reactor Volume. Ind. Eng. Chem. Res. 57, 6048–6056. URL: https://doi.org/10.1021/acs.iecr.7b05091, doi:10.1021/acs.iecr.7b05091.

Valley, L.M., Legvold, S., 1962. Sound Dispersion in Ethane-Ethylene Mixtures and in Halo-Ethane Gases. J. Chem. Phys. 36, 481–485. URL: http://aip.scitation.org/doi/10.1063/1.1732536, doi:10.1063/1.1732536.

Wang, B., Albarracín-Suazo, S., Pagán-Torres, Y., Nikolla, E., 2017. Advances in methane conversion processes. Catal. Today 285, 147 – 158. URL: http://www.sciencedirect.com/science/article/pii/S0920586117300226, doi:10.1016/j.cattod.2017.01.023.

Wang, B., Yan, W., Ge, W., Duan, X., 2013. Methane conversion into higher hydrocarbons with dielectric barrier discharge micro-plasma reactor. J. Energy Chem. 22, 876–882. URL: http://linkinghub.elsevier.com/retrieve/pii/S2095495614602679, doi:10.1016/S2095-4956(14)60267-9.

Wang, J.C.F., Springer, G.S., 1973. Vibrational relaxation times in some hydrocarbons in the range 300–900°K. J. Chem. Phys. 59, 6556–6562. URL: http://aip.scitation.org/doi/10.1063/1.1680034, doi:10.1063/1.1680034.

Wang, W., Berthelot, A., Zhang, Q., Bogaerts, A., 2018. Modelling of plasma-based dry reforming: how do uncertainties in the input data affect the calculation results? J. Phys. D Appl. Phys. 51, 204003. URL: https://doi.org/10.1088%2F1361-6463%2Faab97a, doi:10.1088/1361-6463/aab97a.

Whitehead, J.C., 2016. Plasma–catalysis: the known knowns, the known unknowns and the unknown unknowns. J. Phys. D Appl. Phys. 49, 243001. URL: http://stacks.iop.org/0022-3727/49/i=24/a=243001?key=crossref.a01992d253206d765950fa5a56ade594, doi:10.1088/0022-3727/49/24/243001.

Xu, C., Tu, X., 2013. Plasma-assisted methane conversion in an atmospheric pressure dielectric barrier discharge reactor. J. Energy Chem. 22, 420–425. URL: http://linkinghub.elsevier.com/retrieve/pii/S2095495613600558, doi:10.1016/S2095-4956(13)60055-8.

Yang, Y., 2003a. Direct Non-oxidative Methane Conversion by Non-thermal Plasma: Experimental Study. Plasma Chem. Plasma P. 23, 283–296. URL: https://link.springer.com/article/10.1023/A:1022968002315, doi:10.1023/A:1022968002315.

Yang, Y., 2003b. Direct Non-oxidative Methane Conversion by Non-thermal Plasma: Modeling Study. Plasma Chem. Plasma Process. 23, 327–346. URL: https://link.springer.com/article/10.1023/A:1022924220062, doi:10.1023/A:1022924220062.

Yao, S.L., Suzuki, E., Meng, N., Nakayama, A., 2002. A High-Efficiency Reactor for the Pulsed Plasma Conversion of Methane. Plasma Chem. Plasma P. 22, 225–237. URL: https://link.springer.com/article/10.1023/A:1014843425384, doi:10.1023/A:1014843425384.

Yarin, A.L., Rovagnati, B., Mashayek, F., Matsoukas, T., 2006. A reaction model for plasma coating of nanoparticles by amorphous carbon layers. J. Appl. Phys. 99, 064310. URL: https://aip.scitation.org/doi/10.1063/1.2183587, doi:10.1063/1.2183587.

Yoon, S.F., Tan, K.H., Rusli, Ahn, J., 2001. Modeling and analysis of hydrogen–methane plasma in electron cyclotron resonance chemical vapor deposition of diamond-like carbon. J. Appl. Phys. 91, 40–47. URL: https://aip.scitation.org/doi/abs/10.1063/1.1421038, doi:10.1063/1.1421038.

Graphical Abstract

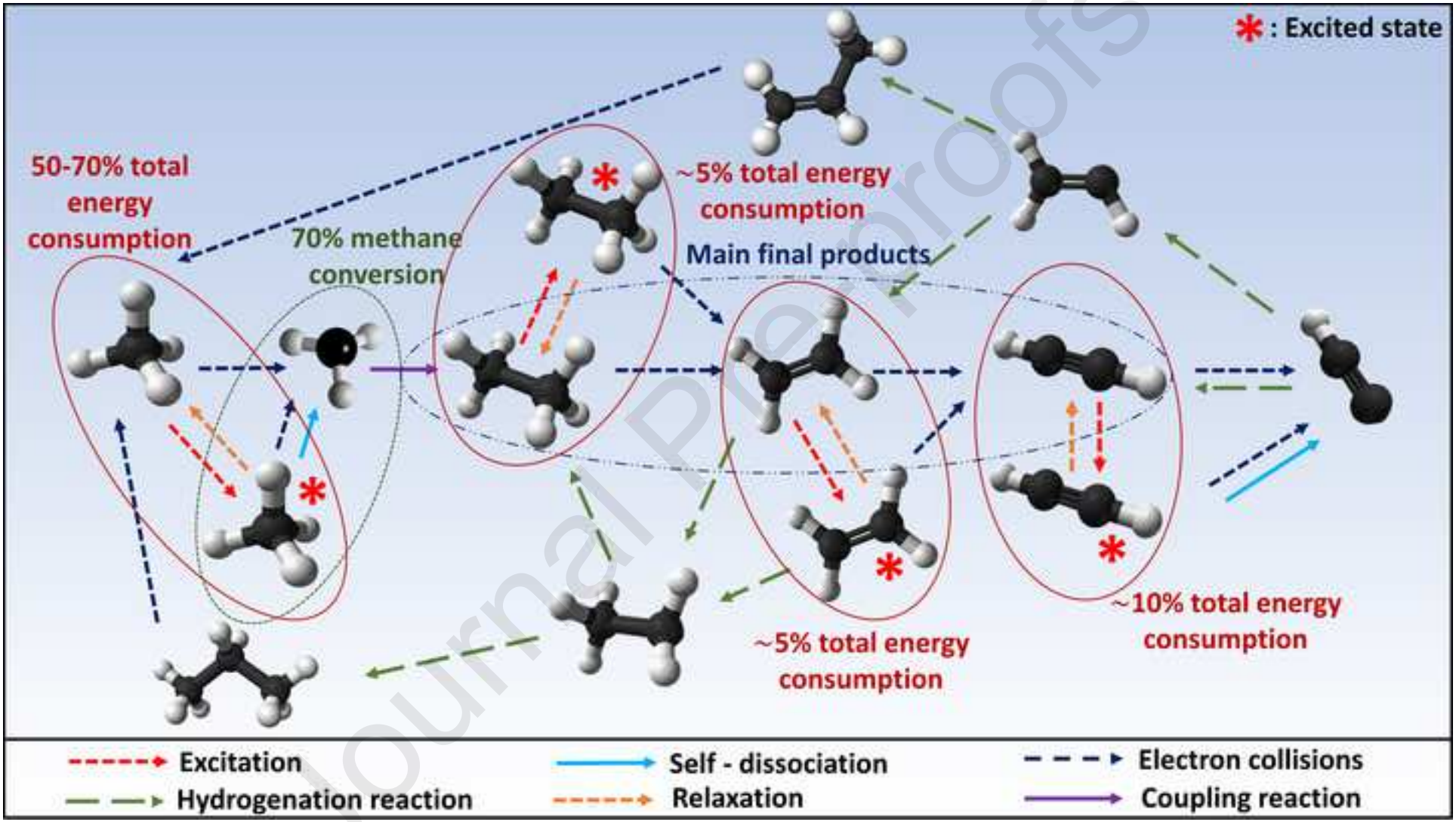

***Highlights**

Highlights

- Detailed kinetic model for non-thermal methane plasma developed
- Reactivity of vibrationally and electronically excited states explicitly considered
- 86% of total energy consumption channelled towards the creation of excited states
- More than 70% of methane conversion takes place via electronically excitation
- Energy relaxation processes comprise the main excited states consumption channels

***Credit Author Statement**

Pierre-André Maitre: Investigation, Methodology, Formal analysis, Data curation, Visualization, Writing - Original Draft. **Matthew S. Bieniek:** Investigation, Methodology, Formal analysis, Writing - Original Draft. **Panagiotis N. Kechagiopoulos:** Conceptualization, Funding acquisition, Project administration, Methodology, Writing - Review & Editing, Supervision.

*Declaration of Interest Statement

Declaration of interests

☒ The authors declare that they have no known competing financial interests or personal relationships that could have appeared to influence the work reported in this paper.

☐The authors declare the following financial interests/personal relationships which may be considered as potential competing interests: